Research in Astronomy and Astrophysics, 24:125015 (19pp), 2024 December https://doi.org/10.1088/1674-4527/ad8ba1

Modeling the Covariance Matrix for the Power Spectra Before and After the BAO Reconstruction

Ruiyang Zhao[1,2,3], Kazuya Koyama[3], Yuting Wang[1,4], and Gong-Bo Zhao[1,2,4,5]
[1] National Astronomical Observatories, Chinese Academy of Sciences, Beijing 100101, China; gbzhao@nao.cas.cn
[2] School of Astronomy and Space Science, University of Chinese Academy of Sciences, Beijing 100049, China
[3] Institute of Cosmology & Gravitation, University of Portsmouth, Dennis Sciama Building, Portsmouth, PO1 3FX, UK
[4] Institute for Frontiers in Astronomy and Astrophysics, Beijing Normal University, Beijing 102206, China
[5] Chinese Academy of Sciences South America Center for Astronomy (CASSACA), National Astronomical Observatories of China, Beijing 100101, China
Received 2024 October 17; revised 2024 October 23; accepted 2024 October 24; published 2024 December 5

Abstract

The baryon acoustic oscillations (BAO) reconstruction plays a crucial role in cosmological analysis for spectroscopic galaxy surveys because it can make the density field effectively more linear and more Gaussian. The combination of the power spectra before and after the BAO reconstruction helps break degeneracies among parameters, then improves the constraints on cosmological parameters. It is therefore important to estimate the covariance matrix between pre- and post-reconstructed power spectra. In this work, we use perturbation theory to estimate the covariance matrix of the related power spectra multipoles, and check the accuracy of the derived covariance model using a large suite of dark matter halo catalogs at $z = 0.5$. We find that the diagonal part of the auto covariance is well described by the Gaussian prediction, while the cross covariance deviates from the Gaussian prediction quickly when $k > 0.1\,h\,\mathrm{Mpc}^{-1}$. Additionally, we find the non-Gaussian effect in the non-diagonal part of the cross covariance is comparable to, or even stronger than, the pre-reconstruction covariance. By adding the non-Gaussian contribution, we obtain good agreement between analytical and numerical covariance matrices in the non-diagonal part up to $k \simeq 0.15\,h\,\mathrm{Mpc}^{-1}$. The agreement in the diagonal part is also improved, but still under-predicts the correlation in the cross covariance block.

Key words: (cosmology:) large-scale structure of universe – cosmology: theory – (cosmology:) cosmological parameters

1. Introduction

The large-scale structure of the Universe carries rich information of the cosmic expansion, the structure growth and primordial physics, and the information leaves imprints on patterns of the three-dimensional (3D) distribution of galaxies such as the baryon acoustic oscillations (BAO; Cole et al. 2005; Eisenstein et al. 2005) and the redshift space distortions (RSD; Kaiser 1987; Peacock et al. 2001), as measured by current and future spectroscopic surveys including Dark Energy Spectroscopic Instrument (DESI; DESI Collaboration et al. 2016), Euclid (Laureijs et al. 2011), Subaru Prime Focus Spectrograph (PFS; Takada et al. 2014), Nancy Grace Roman Space Telescope (Roman; Wang et al. 2022), MegaMapper (Schlegel et al. 2022), and so forth. Given the large number of galaxies, the observational data are usually compressed and analyzed at the 2-point statistics level such as the 2-point correlation function and the power spectrum. The 2-point statistics capture the leading order information of the galaxy density field, and have been well modeled in theory (e.g., Crocce & Scoccimarro 2006; Taruya et al. 2010; Baumann et al. 2012; Carrasco et al. 2012; Vlah et al. 2015; Maus et al. 2024a), and measured and analyzed over the last decades (e.g., Beutler et al. 2011; Alam et al. 2017; D'Amico et al. 2020; Ivanov et al. 2020; Alam et al. 2021; Adame et al. 2024a, 2024b).

To fully exploit the information from galaxy surveys, there have been attempts to measure and model high-order statistics (Gil-Marín et al. 2017; Desjacques et al. 2018; Pearson & Samushia 2018; Eggemeier et al. 2019; Sugiyama et al. 2019; Gualdi et al. 2021; Philcox et al. 2021, 2022; Novell-Masot et al. 2023; Spaar & Zhang 2023; Sugiyama et al. 2023; Wang et al. 2023; Behera et al. 2024; Chen et al. 2024a; D'Amico et al. 2024; Hahn et al. 2024; Leonard et al. 2024). These analyses are, however, much more challenging compared to the 2-point statistics because of the high dimensionality of the observable.

The reconstruction technique (Eisenstein et al. 2007) was proposed to improve the BAO measurement by undoing the large-scale bulk flow which blurred the BAO feature. Although it was originally designed to improve the BAO signal, reconstruction, which is in effect a field level operation, utilizes the higher-order information (Schmittfull et al. 2015) to restore the linear modes that are contaminated by the nonlinear gravitational evolution. Therefore, cosmological information,

such as RSD (Zhu et al. 2018; Hikage et al. 2020a), primordial non-Gaussianity (Shirasaki et al. 2021; Flöss & Meerburg 2024) and the neutrino mass (Zang & Zhu 2024), can in principle be better constrained by analyzing the post-reconstruction sample compared to the pre-reconstruction one when stopped at the same order of n-point statistics. Over the past few years, theoretical studies of the reconstructed field have been mainly focusing on modeling the signal (see White 2015; Seo et al. 2016; Hikage et al. 2017, 2020a; Chen et al. 2019; Ota et al. 2021; Chen et al. 2024b; Sugiyama 2024a, 2024b, 2024c). Recently, Wang et al. (2024b, 2024a) show the combination of pre- and post-reconstructed BAO or power spectra breaks degeneracies among parameters and significantly improves the constraints on cosmological parameters. In this case, it is also important to understand the covariance matrix between pre- and post-reconstructed power spectra because it is nearly singular at small k.

The standard way to estimate the covariance matrix is based on numerical simulations. There are, however, a few disadvantages. First, the finite number of simulations introduces noise into the numerical covariance matrix. The matrix is likely to be ill-formed when observables are highly correlated. Moreover, the noise in the inverse covariance matrix estimation has to be accounted for (Hartlap et al. 2007) and be propagated to model parameters (Percival et al. 2014, 2022), weakening the final cosmological constraints. Second, limited by the computational resources, running a large number of full N-body simulations is usually not available and one has to rely on fast approximated mocks (e.g., Feng et al. 2016; Kitaura et al. 2016; Zhao et al. 2021). Although they are usually well calibrated at the 2-pt statistics level, it is not entirely clear how much they are able to match the higher order statistics (Philcox & Ereza 2024). On the other hand, the perturbation theory provides a clean way to understand all related effects in the covariance matrix calculation (Meiksin & White 1999; Scoccimarro et al. 1999; Bertolini et al. 2016; Chan & Blot 2017; Mohammed et al. 2017; Sugiyama et al. 2020; Wadekar & Scoccimarro 2020). It also provides the ability to perform a quick cross-check with the numerical covariance matrix (Wadekar et al. 2020).

This paper extends the results in Hikage et al. (2020b) to include the galaxy bias and the discreteness effect based on perturbation theory and compute the analytic covariance matrix. In addition, we also model the cross covariance matrix between pre- and post-reconstruction power spectra. We compare the analytic covariance against numerical ones computed from 15,000 Quijote simulations (Villaescusa-Navarro et al. 2020).

This paper is organized as follows. Section 2 presents the analytic covariance matrix model. In Section 3, we compare our analytic covariance matrix model to the numerical one computed from 15,000 Quijote simulations. The conclusions and discussions are summarized in Section 4.

2. The Covariance Matrix Model

2.1. Density Fluctuations and Correlators

Following the counts in the cell formalism in Feldman et al. (1994), Smith (2009) and Sugiyama (2024c), we can divide the simulation box into infinitesimal cells with volume δV. The number of galaxies[6] in the i-th cell, or the galaxy occupation number $n_{g,i}$, is either 0 or 1, satisfying

$$n_{g,i} = n_{g,i}^n, \tag{1}$$

where $n \geqslant 2$. The galaxy number density in the simulation box is then expressed as

$$n_g(\boldsymbol{x}) = \sum_i n_{g,i}\delta_D(\boldsymbol{x} - \boldsymbol{x}_i), \tag{2}$$

with δ_D the Dirac delta function and $\boldsymbol{x}_i$ the position of the i-th cell. The expectation value of the occupation number is $\langle n_{g,i}\rangle = \bar{n}_g\delta V$, with $\bar{n}_g$ the galaxy number density. Assuming galaxies are distributed following the Poisson point process, the occupation numbers in different cells ($i \neq j \neq k \neq l$) are only correlated through the underlying continuous galaxy density field

$$\langle n_{g,i}n_{g,j}\rangle_c = \bar{n}_g^2\xi_{gg}(\boldsymbol{x}_i, \boldsymbol{x}_j)\delta V^2, \tag{3}$$

$$\langle n_{g,i}n_{g,j}n_{g,k}\rangle_c = \bar{n}_g^3\zeta_{ggg}(\boldsymbol{x}_i, \boldsymbol{x}_j, \boldsymbol{x}_k)\delta V^3, \tag{4}$$

$$\langle n_{g,i}n_{g,j}n_{g,k}n_{g,l}\rangle_c = \bar{n}_g^4\eta_{gggg}(\boldsymbol{x}_i, \boldsymbol{x}_j, \boldsymbol{x}_k, \boldsymbol{x}_l)\delta V^4, \tag{5}$$

where we use notation $\langle\cdots\rangle_c$ to represent the cumulant average, and we have defined the two-, three- and four-point galaxy correlation functions ξ_{gg}, ζ_{ggg} and η_{gggg}, respectively.

In Fourier space, the galaxy number density becomes

$$n_g(\boldsymbol{k}) = \sum_i n_{g,i}e^{-i\boldsymbol{k}\cdot\boldsymbol{x}_i}. \tag{6}$$

For the convenience of later calculations, we can define

$$\delta_{g,i}(\boldsymbol{k}) = \frac{1}{\bar{n}_g}n_{g,i}e^{-i\boldsymbol{k}\cdot\boldsymbol{x}_i}. \tag{7}$$

The summation of $\delta_{g,i}$ satisfies

$$\begin{aligned}\sum_i\langle\delta_{g,i}(\boldsymbol{k})\rangle_c &= \frac{1}{\bar{n}_g}\sum_i\langle n_{g,i}\rangle_c e^{-i\boldsymbol{k}\cdot\boldsymbol{x}_i}\\ &= \sum_i e^{-i\boldsymbol{k}\cdot\boldsymbol{x}_i}\delta V \to \int_V e^{-i\boldsymbol{k}\cdot\boldsymbol{x}}\mathrm{d}^3x = V\delta_{\boldsymbol{k}}^K,\end{aligned} \tag{8}$$

where V is the volume of the simulation box, and $\delta_{\boldsymbol{k}}^K$ is the Kronecker delta symbol, which is equal to 1 when $\boldsymbol{k} = \boldsymbol{0}$ and vanishes otherwise. Here the arrow indicates that we take the continuous limit. The 2-point correlation of $\delta_{g,i}$ is

$$\sum_{i\neq j}\langle\delta_{g,i}(\boldsymbol{k}_1)\delta_{g,j}(\boldsymbol{k}_2)\rangle_c = \sum_{i\neq j}\xi_{gg}(\boldsymbol{x}_i, \boldsymbol{x}_j)e^{-i\boldsymbol{k}_1\cdot\boldsymbol{x}_i}e^{-i\boldsymbol{k}_2\cdot\boldsymbol{x}_j}\delta V^2 \tag{9}$$

[6] Our derivations in this section also apply to halos, so we will use "galaxy" and "halo" interchangeably in the later section.

$$\rightarrow \int_V e^{-i(\boldsymbol{k}_1+\boldsymbol{k}_2)\cdot\boldsymbol{x}_2}\mathrm{d}^3x_2 \int_V \xi_{gg}(|\boldsymbol{x}_1-\boldsymbol{x}_2|) \times e^{-i\boldsymbol{k}_1\cdot(\boldsymbol{x}_1-\boldsymbol{x}_2)}\mathrm{d}^3|\boldsymbol{x}_1-\boldsymbol{x}_2| = V\delta^K_{\boldsymbol{k}_{12}}P_{gg}(\boldsymbol{k}_1), \quad (10)$$

where P_{gg} is the power spectrum, and we use the notation $\boldsymbol{k}_{12}\equiv\boldsymbol{k}_1+\boldsymbol{k}_2$. Similarly, higher order correlations of $\delta_{g,i}$ are related to bispectrum and trispectrum, respectively,

$$\sum_{i\neq j\neq k}\langle\delta_{g,i}(\boldsymbol{k}_1)\delta_{g,j}(\boldsymbol{k}_2)\delta_{g,j}(\boldsymbol{k}_3)\rangle_c = V\delta^K_{\boldsymbol{k}_{123}}B_{ggg}(\boldsymbol{k}_1,\boldsymbol{k}_2,\boldsymbol{k}_3), \quad (11)$$

$$\sum_{i\neq j\neq k\neq l}\langle\delta_{g,i}(\boldsymbol{k}_1)\delta_{g,j}(\boldsymbol{k}_2)\delta_{g,j}(\boldsymbol{k}_3)\delta_{g,l}(\boldsymbol{k}_4)\rangle_c = V\delta^K_{\boldsymbol{k}_{1234}}T_{gggg}(\boldsymbol{k}_1,\boldsymbol{k}_2,\boldsymbol{k}_3,\boldsymbol{k}_4). \quad (12)$$

2.2. The Shot Noise Effect

Correlation of occupation numbers in the same cell is called the discreteness effect or the shot noise effect. It can be evaluated using Equation (1), or equivalently

$$\delta_{g,i}(\boldsymbol{k}_1)\delta_{g,i}(\boldsymbol{k}_2) = \frac{1}{\bar{n}_g}\delta_{g,i}(\boldsymbol{k}_{12}). \quad (13)$$

We will use the superscript N to represent correlators with the shot noise effect, i.e.,

$$\sum_{i,j}\langle\delta_{g,i}(\boldsymbol{k}_1)\delta_{g,j}(\boldsymbol{k}_2)\rangle_c = V\delta^K_{\boldsymbol{k}_{12}}P^{\mathrm{N}}_{gg}(\boldsymbol{k}_1) \quad (14)$$

$$\sum_{i,j,k}\langle\delta_{g,i}(\boldsymbol{k}_1)\delta_{g,j}(\boldsymbol{k}_2)\delta_{g,k}(\boldsymbol{k}_3)\rangle_c = V\delta^K_{\boldsymbol{k}_{123}}B^{\mathrm{N}}_{ggg}(\boldsymbol{k}_1,\boldsymbol{k}_2,\boldsymbol{k}_3) \quad (15)$$

$$\sum_{i,j,k,l}\langle\delta_{g,i}(\boldsymbol{k}_1)\delta_{g,j}(\boldsymbol{k}_2)\delta_{g,k}(\boldsymbol{k}_3)\delta_{g,l}(\boldsymbol{k}_4)\rangle_c = V\delta^K_{\boldsymbol{k}_{1234}}T^{\mathrm{N}}_{gggg}(\boldsymbol{k}_1,\boldsymbol{k}_2,\boldsymbol{k}_3,\boldsymbol{k}_4). \quad (16)$$

The following expression is also useful in the later calculation

$$\sum_{i\neq j,k}\langle\delta_{g,i}(\boldsymbol{k}_1)\delta_{g,j}(\boldsymbol{k}_2)\delta_{g,k}(\boldsymbol{k}_3)\rangle_c = V\delta^K_{\boldsymbol{k}_{123}}B^{\mathrm{N12}}_{ggg}(\boldsymbol{k}_1,\boldsymbol{k}_2,\boldsymbol{k}_3). \quad (17)$$

Here the superscript N12 indicates that the correlation between the first and the second density field in the same cell is removed, i.e., the shot noise effect is partially removed in this correlator. Their explicit expressions are given in Appendix.

2.3. The BAO Reconstruction

In the standard Zeldovich reconstruction, the density field after reconstruction n_* reads

$$n_*(\boldsymbol{x}) = n_d(\boldsymbol{x}) - \alpha n_s(\boldsymbol{x}), \quad (18)$$

where α is the ratio of the total number of galaxies to randoms, n_d is the displaced data number density, and n_s is the displaced random number density. They are obtained by moving particles in the galaxy catalog n_g and an initially unclustered catalog consists of random particles n_r according to the shift field $\boldsymbol{s}(\boldsymbol{x})$.

The shift field in Fourier space can be explicitly written as

$$\boldsymbol{s}(\boldsymbol{k}) = i\boldsymbol{R}(\boldsymbol{k})\delta_g(\boldsymbol{k}). \quad (19)$$

Here δ_g is the galaxy overdensity field $\delta_g(\boldsymbol{x}) = n_g(\boldsymbol{x})/\bar{n}_g - 1$, while kernel $\boldsymbol{R}$ determines the reconstruction detail

$$\boldsymbol{R}(\boldsymbol{k}) = -\frac{\boldsymbol{k}+f_{\mathrm{fid}}(\boldsymbol{k}\cdot\hat{\boldsymbol{\eta}})\hat{\boldsymbol{\eta}}}{k^2}\frac{\mathcal{S}(k)}{b_{\mathrm{fid}}+f_{\mathrm{fid}}(\hat{\boldsymbol{k}}\cdot\hat{\boldsymbol{\eta}})^2}, \quad (20)$$

where f_{fid} is the fiducial growth rate, b_{fid} is the fiducial linear galaxy bias, $\hat{\boldsymbol{\eta}}$ is the line-of-sight and $\mathcal{S}$ is the smoothing kernel, whose functional form is given by

$$\mathcal{S}(\boldsymbol{k}) = \exp\{-k^2\Sigma_s^2/2\}, \quad (21)$$

with Σ_s the smoothing scale.

The continuity equation implies

$$n_d(\boldsymbol{x}) = \int \mathrm{d}^3x' n_g(\boldsymbol{x}')\delta_D(\boldsymbol{x}-\boldsymbol{x}'-\boldsymbol{s}(\boldsymbol{x}')), \quad (22)$$

$$n_s(\boldsymbol{x}) = \int \mathrm{d}^3x' n_r(\boldsymbol{x}')\delta_D(\boldsymbol{x}-\boldsymbol{x}'-\boldsymbol{s}(\boldsymbol{x}')). \quad (23)$$

In Fourier space, they become

$$n_d(\boldsymbol{k}) = \int \mathrm{d}^3x\ n_g(\boldsymbol{x})e^{-i\boldsymbol{k}\cdot[\boldsymbol{x}+\boldsymbol{s}(\boldsymbol{x})]}$$
$$n_s(\boldsymbol{k}) = \int \mathrm{d}^3x\ n_r(\boldsymbol{x})e^{-i\boldsymbol{k}\cdot[\boldsymbol{x}+\boldsymbol{s}(\boldsymbol{x})]}. \quad (24)$$

Expanding the exponential term, we can then relate the reconstructed overdensity field δ_* with the galaxy and random overdensity field (Shirasaki et al. 2021)

$$\delta_*(\boldsymbol{k}) = \frac{n_d(\boldsymbol{k})-\alpha n_s(\boldsymbol{k})}{\bar{n}_g}, \quad (25)$$

$$\equiv \int \mathrm{d}^3x\ [\delta_g(\boldsymbol{x})-\delta_r(\boldsymbol{x})]e^{-i\boldsymbol{k}\cdot[\boldsymbol{x}+\boldsymbol{s}(\boldsymbol{x})]}, \quad (26)$$

$$= \sum_{n=0}^{\infty}\frac{1}{n!}\int_{\boldsymbol{k}=\boldsymbol{p}_{1\cdots n+1}}[\boldsymbol{k}\cdot\boldsymbol{R}(\boldsymbol{p}_2)]\cdots[\boldsymbol{k}\cdot\boldsymbol{R}(\boldsymbol{p}_{n+1})] \times[\delta_g(\boldsymbol{p}_1)-\delta_r(\boldsymbol{p}_1)]\delta_g(\boldsymbol{p}_2)\cdots\delta_g(\boldsymbol{p}_{n+1}), \quad (27)$$

$$\simeq \sum_{n=0}^{\infty}\frac{1}{n!}\int_{\boldsymbol{k}=\boldsymbol{p}_{1\cdots n+1}}[\boldsymbol{k}\cdot\boldsymbol{R}(\boldsymbol{p}_2)]\cdots[\boldsymbol{k}\cdot\boldsymbol{R}(\boldsymbol{p}_{n+1})] \times\delta_g(\boldsymbol{p}_1)\delta_g(\boldsymbol{p}_2)\cdots\delta_g(\boldsymbol{p}_{n+1}), \quad (28)$$

$$= \sum_{n=1}^{\infty}\int_{\boldsymbol{k}=\boldsymbol{p}_{1\cdots n}}R_n(\boldsymbol{p}_1,\cdots\boldsymbol{p}_n)\delta_g(\boldsymbol{p}_1)\cdots\delta_g(\boldsymbol{p}_n), \quad (29)$$

where we use the notation

$$\int_{\boldsymbol{k}=\boldsymbol{p}_{1\cdots n}} \equiv \int\frac{\mathrm{d}^3p_1}{(2\pi)^3}\cdots\int\frac{\mathrm{d}^3p_n}{(2\pi)^3}(2\pi)^3\delta_D(\boldsymbol{k}-\boldsymbol{p}_{1\cdots n}). \quad (30)$$

The overdensity of randoms is defined by $\delta_r(\boldsymbol{x})\equiv\alpha n_r(\boldsymbol{x})/\bar{n}_g - 1$, and has been neglected in the final expression. This is because the contribution from δ_r is generally $\alpha\sim 1/50$ times smaller compared to that from δ_g. For example, in the shot noise dominated region we have $P^{\mathrm{N}}_{rr} = \alpha P^{\mathrm{N}}_{gg}$. The last line defines the n-th order symmetrized reconstruction kernel. The

first three terms are given by

$$R_1(\boldsymbol{p}_1) = 1, \tag{31}$$

$$R_2(\boldsymbol{p}_1, \boldsymbol{p}_2) = \frac{1}{2}\boldsymbol{p}_{12} \cdot [\boldsymbol{R}(\boldsymbol{p}_1) + \boldsymbol{R}(\boldsymbol{p}_2)], \tag{32}$$

$$R_3(\boldsymbol{p}_1, \boldsymbol{p}_2, \boldsymbol{p}_3) = \frac{1}{6}\{[\boldsymbol{p}_{123} \cdot \boldsymbol{R}(\boldsymbol{p}_1)][\boldsymbol{p}_{123} \cdot \boldsymbol{R}(\boldsymbol{p}_2)] + (2 \text{ cyc.})\}. \tag{33}$$

Analogous to the galaxy number density, the discrete form of random number density is described by

$$n_r(\boldsymbol{x}) = \sum_i n_{r,i}\delta_D(\boldsymbol{x} - \boldsymbol{x}_i), \tag{34}$$

where $n_{r,i}$ is the random occupation number satisfying $n_{r,i} = n_{r,i}^2$. In addition, since the generation of random catalogs is independent of galaxies, galaxies and randoms are never in the same cell, i.e.,

$$n_{g,i}n_{r,i} = 0. \tag{35}$$

n_d, n_s and n_* can then be expressed in discrete forms

$$n_d(\boldsymbol{x}) = \sum_i n_{g,i}\delta_D(\boldsymbol{x} - \boldsymbol{x}_i - \boldsymbol{s}_i) \quad n_d(\boldsymbol{k}) = \sum_i n_{g,i}e^{-i\boldsymbol{k}\cdot(\boldsymbol{x}_i+\boldsymbol{s}_i)}, \tag{36}$$

$$n_s(\boldsymbol{x}) = \sum_i n_{r,i}\delta_D(\boldsymbol{x} - \boldsymbol{x}_i - \boldsymbol{s}_i) \quad n_s(\boldsymbol{k}) = \sum_i n_{r,i}e^{-i\boldsymbol{k}\cdot(\boldsymbol{x}_i+\boldsymbol{s}_i)}, \tag{37}$$

$$\begin{aligned} n_*(\boldsymbol{x}) &= \sum_i (n_{g,i} - \alpha n_{r,i})\delta_D(\boldsymbol{x} - \boldsymbol{x}_i - \boldsymbol{s}_i) \\ n_*(\boldsymbol{k}) &= \sum_i (n_{g,i} - \alpha n_{r,i})e^{-i\boldsymbol{k}\cdot(\boldsymbol{x}_i+\boldsymbol{s}_i)}, \end{aligned} \tag{38}$$

with $\boldsymbol{s}_i$ the shift field evaluated at the position of the i-th cell. Using the notation

$$\delta_{*,i} = \frac{1}{\bar{n}_g}(n_{g,i} - \alpha n_{r,i})e^{-i\boldsymbol{k}\cdot(\boldsymbol{x}_i+\boldsymbol{s}_i)}, \tag{39}$$

the post-reconstruction power spectrum, bispectrum and trispectrum are defined as follows

$$\sum_{i\neq j}\langle\delta_{*,i}(\boldsymbol{k}_1)\delta_{*,j}(\boldsymbol{k}_2)\rangle_c = V\delta^K_{\boldsymbol{k}_{12}}P_{**}(\boldsymbol{k}_1), \tag{40}$$

$$\sum_{i\neq j\neq k}\langle\delta_{*,i}(\boldsymbol{k}_1)\delta_{*,j}(\boldsymbol{k}_2)\delta_{*,k}(\boldsymbol{k}_3)\rangle_c = V\delta^K_{\boldsymbol{k}_{123}}B_{***}(\boldsymbol{k}_1, \boldsymbol{k}_2, \boldsymbol{k}_3), \tag{41}$$

$$\sum_{i\neq j\neq k\neq l}\langle\delta_{*,i}(\boldsymbol{k}_1)\delta_{*,j}(\boldsymbol{k}_2)\delta_{*,k}(\boldsymbol{k}_3)\delta_{*,l}(\boldsymbol{k}_4)\rangle_c = V\delta^K_{\boldsymbol{k}_{1234}}T_{****}(\boldsymbol{k}_1, \boldsymbol{k}_2, \boldsymbol{k}_3, \boldsymbol{k}_4). \tag{42}$$

Their shot noise effect including counterparts and cross-correlations between pre- and post-reconstruction density field can be very similarly defined.

2.4. The Shot Noise Effect After Reconstruction

Contrary to the pre-reconstruction case, the shot noise effect, even if Poissonian, cannot be removed by subtracting the self-pair contribution. Sugiyama (2024c) developed a method to compute the shot noise effect by counting self-pairs in the galaxy density field. We will follow this approach and derive the impact on bispectrum and trispectrum.

We only need to expand δ_* up to the 3rd order as we are only interested in the tree-level bispectrum and trispectrum

$$\begin{aligned} \delta_*(\boldsymbol{k}) = &\sum_i \delta_{g,i}(\boldsymbol{k}) + \sum_{i,i'}\int_{\boldsymbol{k}=\boldsymbol{p}_{12}} R_2(\boldsymbol{p}_1, \boldsymbol{p}_2)\delta_{g,i}(\boldsymbol{p}_1)\delta_{g,i'}(\boldsymbol{p}_2) \\ &+ \sum_{i,i',i''}\int_{\boldsymbol{k}=\boldsymbol{p}_{123}} R_3(\boldsymbol{p}_1, \boldsymbol{p}_2, \boldsymbol{p}_3)\delta_{g,i}(\boldsymbol{p}_1)\delta_{g,i'}(\boldsymbol{p}_2)\delta_{g,i''}(\boldsymbol{p}_3) \\ &+ \mathcal{O}(\delta_g^4). \end{aligned} \tag{43}$$

The calculation is then very similar to the pre-reconstruction galaxy bispectrum and trispectrum, except that we need to differentiate between the shot noise included and excluded correlators when connecting internal legs in the diagram. For example, the first line of Figure 1 shows the diagram of B_{***}, where internal legs represent δ_g while external legs represent δ_*. Filled circles signify galaxy correlators without the shot noise effect, while empty circles include the shot noise. Therefore, the post-reconstruction bispectrum is given by

$$\begin{aligned} B_{***}(\boldsymbol{k}_1, \boldsymbol{k}_2, \boldsymbol{k}_3) = &R_1(\boldsymbol{k}_1)R_1(\boldsymbol{k}_2)R_1(\boldsymbol{k}_3)B_{ggg}(\boldsymbol{k}_1, \boldsymbol{k}_2, \boldsymbol{k}_3) \\ &+ \{R_2(-\boldsymbol{k}_2, -\boldsymbol{k}_3)R_1(\boldsymbol{k}_2)R_1(\boldsymbol{k}_3) \\ &\times [P_{gg}(\boldsymbol{k}_2)P^{\rm N}_{gg}(\boldsymbol{k}_3) + (\boldsymbol{k}_2 \leftrightarrow \boldsymbol{k}_3)] + (2 \text{ cyc.})\}. \end{aligned} \tag{44}$$

This expression recovers Equation (22) in Shirasaki et al. (2021) if we rewrite R_2 in terms of the perturbation kernel $Z_2^{\rm rec}$ after reconstruction.

The cross-correlation can be similarly obtained as

$$\begin{aligned} B_{g**}(\boldsymbol{k}_1, \boldsymbol{k}_2, \boldsymbol{k}_3) = &R_1(\boldsymbol{k}_2)R_1(\boldsymbol{k}_3)B_{ggg}(\boldsymbol{k}_1, \boldsymbol{k}_2, \boldsymbol{k}_3) \\ &+ \{R_2(-\boldsymbol{k}_1, -\boldsymbol{k}_2)R_1(\boldsymbol{k}_2)[P_{gg}(\boldsymbol{k}_1)P^{\rm N}_{gg}(\boldsymbol{k}_2), \\ &+ (\boldsymbol{k}_1 \leftrightarrow \boldsymbol{k}_2)] + (\boldsymbol{k}_2 \leftrightarrow \boldsymbol{k}_3)\} \end{aligned} \tag{45}$$

$$\begin{aligned} B_{gg*}(\boldsymbol{k}_1, \boldsymbol{k}_2, \boldsymbol{k}_3) = &R_1(\boldsymbol{k}_3)B_{ggg}(\boldsymbol{k}_1, \boldsymbol{k}_2, \boldsymbol{k}_3) \\ &+ R_2(-\boldsymbol{k}_1, -\boldsymbol{k}_2)R_1(\boldsymbol{k}_3)[P_{gg}(\boldsymbol{k}_1)P^{\rm N}_{gg}(\boldsymbol{k}_2) + (\boldsymbol{k}_1 \leftrightarrow \boldsymbol{k}_2)]. \end{aligned} \tag{46}$$

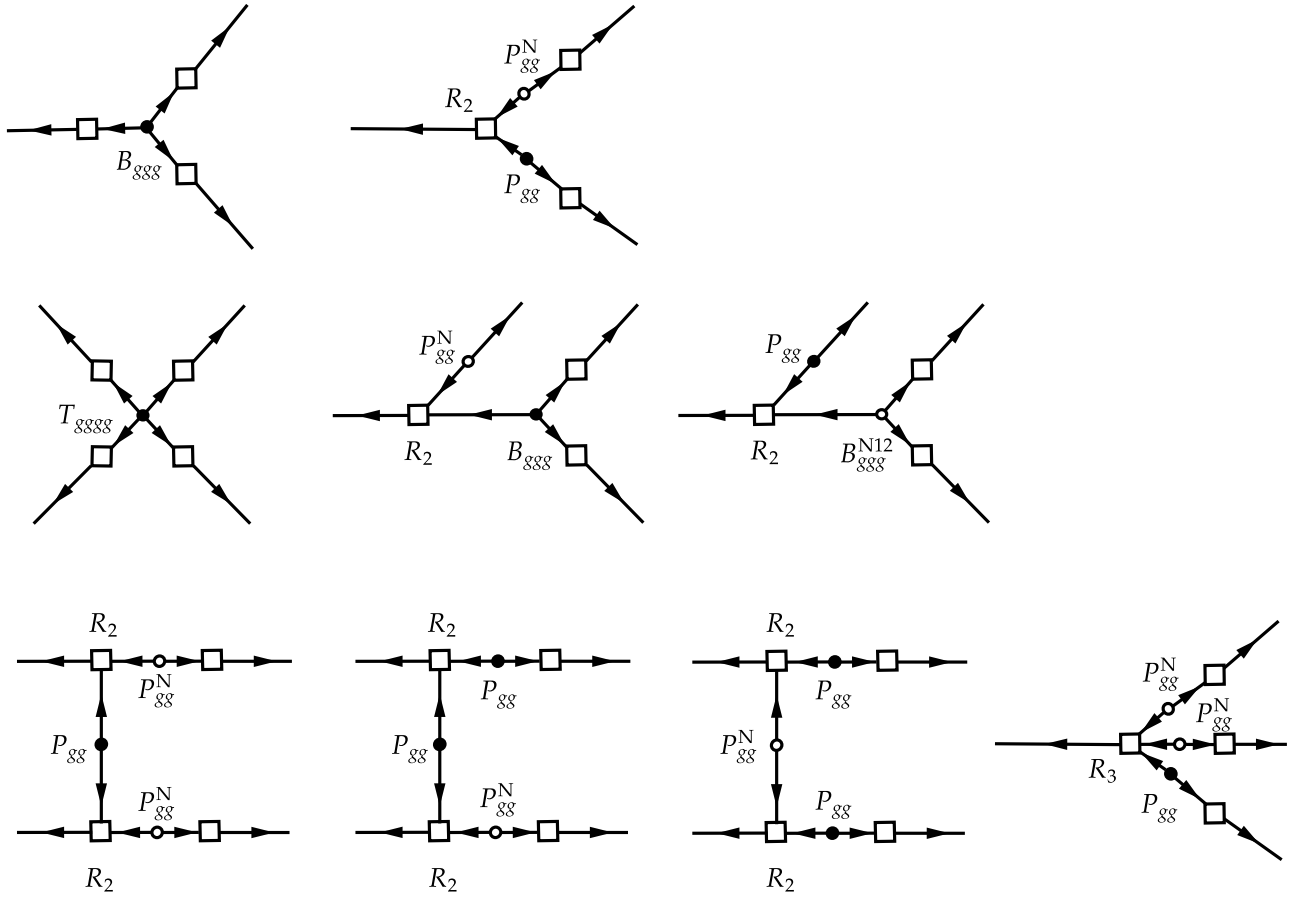

Figure 1. Diagram of post-reconstruction bispectrum B_{***} and trispectrum T_{****}.

The 2nd and 3rd lines of Figure 1 show the diagram of the post-reconstruction trispectrum, which gives

$$
\begin{aligned}
&T_{****}(\boldsymbol{k}_1, \boldsymbol{k}_2, \boldsymbol{k}_3, \boldsymbol{k}_4)\\
&= R_1(\boldsymbol{k}_1)R_1(\boldsymbol{k}_2)R_1(\boldsymbol{k}_3)R_1(\boldsymbol{k}_4)T_{gggg}(\boldsymbol{k}_1, \boldsymbol{k}_2, \boldsymbol{k}_3, \boldsymbol{k}_4)\\
&\quad + R_2(-\boldsymbol{k}_2, \boldsymbol{k}_1 + \boldsymbol{k}_2)R_1(\boldsymbol{k}_2)R_1(\boldsymbol{k}_3)R_1(\boldsymbol{k}_4)\\
&\quad \times [P^{\rm N}_{gg}(\boldsymbol{k}_2)B_{ggg}(\boldsymbol{k}_3, \boldsymbol{k}_4, \boldsymbol{k}_1 + \boldsymbol{k}_2)\\
&\quad + P_{gg}(\boldsymbol{k}_2)B^{\rm N12}_{ggg}(\boldsymbol{k}_3, \boldsymbol{k}_4, \boldsymbol{k}_1 + \boldsymbol{k}_2)] + (11\ \text{perm.})\\
&\quad + R_2(-\boldsymbol{k}_4, \boldsymbol{k}_1 + \boldsymbol{k}_4)R_2(-\boldsymbol{k}_3, \boldsymbol{k}_2 + \boldsymbol{k}_3)R_1(\boldsymbol{k}_3)R_1(\boldsymbol{k}_4)\\
&\quad \times [P^{\rm N}_{gg}(\boldsymbol{k}_4)P^{\rm N}_{gg}(\boldsymbol{k}_3)P_{gg}(\boldsymbol{k}_1 + \boldsymbol{k}_4)\\
&\quad + P^{\rm N}_{gg}(\boldsymbol{k}_4)P_{gg}(\boldsymbol{k}_3)P^{\rm N}_{gg}(\boldsymbol{k}_1 + \boldsymbol{k}_4)\\
&\quad + P_{gg}(\boldsymbol{k}_4)P^{\rm N}_{gg}(\boldsymbol{k}_3)P^{\rm N}_{gg}(\boldsymbol{k}_1 + \boldsymbol{k}_4)\\
&\quad + P_{gg}(\boldsymbol{k}_4)P_{gg}(\boldsymbol{k}_3)P^{\rm N}_{gg}(\boldsymbol{k}_1 + \boldsymbol{k}_4)] + (11\ \text{perm.})\\
&\quad + R_3(\boldsymbol{k}_2, \boldsymbol{k}_3, \boldsymbol{k}_4)R_1(\boldsymbol{k}_2)R_1(\boldsymbol{k}_3)R_1(\boldsymbol{k}_4)\\
&\quad \times [2P_{gg}(\boldsymbol{k}_2)P^{\rm N}_{gg}(\boldsymbol{k}_3)P^{\rm N}_{gg}(\boldsymbol{k}_4) + (2\ \text{cyc.})] + (3\ \text{cyc.}). \qquad (47)
\end{aligned}
$$

Similarly, the cross-correlation trispectrum with the full shot noise effect is given by

$$
\begin{aligned}
&T^{\rm N}_{gg**}(\boldsymbol{k}_1, \boldsymbol{k}_2, \boldsymbol{k}_3, \boldsymbol{k}_4) = R_1(\boldsymbol{k}_3)R_1(\boldsymbol{k}_4)T^{\rm N}_{gggg}(\boldsymbol{k}_1, \boldsymbol{k}_2, \boldsymbol{k}_3, \boldsymbol{k}_4)\\
&\quad + \{[2R_2(-\boldsymbol{k}_1, -\boldsymbol{k}_{23})P^{\rm N}_{gg}(\boldsymbol{k}_1)B^{\rm N}_{ggg}(\boldsymbol{k}_2, \boldsymbol{k}_3, -\boldsymbol{k}_{23})\\
&\quad + (2\ \text{cyc.})] + (\boldsymbol{k}_3 \leftrightarrow \boldsymbol{k}_4)\}\\
&\quad + \{4R_2(-\boldsymbol{k}_1, -\boldsymbol{k}_{23})R_2(-\boldsymbol{k}_2, \boldsymbol{k}_{23})P^{\rm N}_{gg}(\boldsymbol{k}_1)P^{\rm N}_{gg}\\
&\quad \times (\boldsymbol{k}_2)P^{\rm N}_{gg}(\boldsymbol{k}_{23}) + (\boldsymbol{k}_1 \leftrightarrow \boldsymbol{k}_2)\}\\
&\quad + \{6R_3(-\boldsymbol{k}_1, -\boldsymbol{k}_2, -\boldsymbol{k}_3)P^{\rm N}_{gg}(\boldsymbol{k}_1)P^{\rm N}_{gg}(\boldsymbol{k}_2)P^{\rm N}_{gg}(\boldsymbol{k}_3)\\
&\quad + (\boldsymbol{k}_3 \leftrightarrow \boldsymbol{k}_4)\}.
\end{aligned} \qquad (48)
$$

Note that the above equations only hold perturbatively, and one should expand P_{gg}, B_{ggg} and T_{gggg} at the tree-level. Although in this work we only assume Poissonian shot noise, the full stochastic term (Perko et al. 2016) can in principle to be

plugged into the above equations or re-parameterized. We refer the readers to Ebina & White (2024a) for a relevant discussion.

2.5. The Gaussian Covariance

The pre- and post-reconstruction power spectrum estimators for an individual mode are given by

$$\hat{P}_{gg}(\boldsymbol{k}) = \frac{1}{V\bar{n}_g^2}\{|n_g(\boldsymbol{k})|^2 - N_g\}, \tag{49}$$

$$\widehat{P}_{**}(\boldsymbol{k}) = \frac{1}{V\bar{n}_g^2}\{|n_*(\boldsymbol{k})|^2 - (1+\alpha)N_g\}, \tag{50}$$

where N_g is the total number of galaxies. These two estimators are shot noise subtracted, and can be expressed in terms of $\delta_{g,i}$ and $\delta_{*,i}$

$$\begin{aligned}\widehat{P}_{gg}(\boldsymbol{k}) &= \frac{1}{V}\sum_{i\neq j}\delta_{g,i}(\boldsymbol{k})\delta_{g,j}(-\boldsymbol{k})\\ \widehat{P}_{**}(\boldsymbol{k}) &= \frac{1}{V}\sum_{i\neq j}\delta_{*,i}(\boldsymbol{k})\delta_{*,j}(-\boldsymbol{k}).\end{aligned} \tag{51}$$

The cross power spectrum estimator between pre- and post-reconstruction density field is written as

$$\widehat{P}^{\rm N}_{g*}(\boldsymbol{k}) = \frac{1}{V\bar{n}_g^2}n_g(\boldsymbol{k})n_*(\boldsymbol{k}) = \frac{1}{V}\sum_{i,j}\delta_{g,i}(\boldsymbol{k})\delta_{*,i}(-\boldsymbol{k}), \tag{52}$$

here we do not subtract the shot noise.

The pre-reconstruction covariance is then given by[7]

$$C_{gggg}(\boldsymbol{k}_1,\boldsymbol{k}_2) = \langle\hat{P}_{gg}(\boldsymbol{k}_1)\hat{P}_{gg}(\boldsymbol{k}_2)\rangle - \langle\hat{P}_{gg}(\boldsymbol{k}_1)\rangle\langle\hat{P}_{gg}(\boldsymbol{k}_2)\rangle, \tag{53}$$

$$\begin{aligned}&= \frac{1}{V^2}\sum_{i,k}\langle\delta_{g,i}(\boldsymbol{k}_1)\delta_{g,k}(\boldsymbol{k}_2)\rangle_c\sum_{j,l}\\ &\times\langle\delta_{g,j}(-\boldsymbol{k}_1)\delta_{g,l}(-\boldsymbol{k}_2)\rangle_c + (\boldsymbol{k}_2\leftrightarrow-\boldsymbol{k}_2)\\ &+\frac{1}{V^2}\sum_{i\neq j,k\neq l}\langle\delta_{g,i}(\boldsymbol{k}_1)\delta_{g,j}(-\boldsymbol{k}_1)\delta_{g,k}(\boldsymbol{k}_2)\delta_{g,l}(-\boldsymbol{k}_2)\rangle_c,\end{aligned} \tag{54}$$

$$\equiv C^{\rm G}_{gggg}(\boldsymbol{k}_1,\boldsymbol{k}_2) + C^{\rm T}_{gggg}(\boldsymbol{k}_1,\boldsymbol{k}_2). \tag{55}$$

The last line defines the Gaussian and non-Gaussian contribution. The Gaussian contribution evaluates as

$$C^{\rm G}_{gggg}(\boldsymbol{k}_1,\boldsymbol{k}_2) = [P^{\rm N}_{gg}(\boldsymbol{k}_1)]^2(\delta^K_{\boldsymbol{k}_1+\boldsymbol{k}_2} + \delta^K_{\boldsymbol{k}_1-\boldsymbol{k}_2}). \tag{56}$$

The post-reconstruction and the cross covariance between pre- and post-reconstruction covariance are similarly given as

$$C^{\rm G}_{****}(\boldsymbol{k}_1,\boldsymbol{k}_2) = [P^{\rm N}_{**}(\boldsymbol{k}_1)]^2(\delta^K_{\boldsymbol{k}_1+\boldsymbol{k}_2} + \delta^K_{\boldsymbol{k}_1-\boldsymbol{k}_2}), \tag{57}$$

$$C^{\rm G}_{gg**}(\boldsymbol{k}_1,\boldsymbol{k}_2) = [P^{\rm N}_{g*}(\boldsymbol{k}_1)]^2(\delta^K_{\boldsymbol{k}_1+\boldsymbol{k}_2} + \delta^K_{\boldsymbol{k}_1-\boldsymbol{k}_2}). \tag{58}$$

[7] Terms involving $\langle\delta_{g,i}(\boldsymbol{k})\rangle_c$ vanish because $k_1\neq 0$ and $k_2\neq 0$.

2.6. The Non-Gaussian Covariance

The non-Gaussian covariance for pre-reconstruction is given by Wadekar & Scoccimarro (2020), Sugiyama et al. (2020). The post-reconstruction covariance has the same structure as the pre-reconstruction one

$$\begin{aligned}C^{\rm T}_{****}(\boldsymbol{k}_1,\boldsymbol{k}_2) &= \frac{1}{V}T_{****}(\boldsymbol{k}_1,-\boldsymbol{k}_1,\boldsymbol{k}_2,-\boldsymbol{k}_2)\\ &+\frac{1}{V}\frac{1}{\bar{n}_g}[B_{***}(\boldsymbol{k}_{12},-\boldsymbol{k}_1,-\boldsymbol{k}_2)\\ &+B_{***}(\boldsymbol{k}_1-\boldsymbol{k}_2,-\boldsymbol{k}_1,\boldsymbol{k}_2) + (\boldsymbol{k}_i\leftrightarrow-\boldsymbol{k}_i)]\\ &+\frac{1}{V}\frac{1}{\bar{n}_g^2}[P_{**}(\boldsymbol{k}_1+\boldsymbol{k}_2) + P_{**}(\boldsymbol{k}_1-\boldsymbol{k}_2)].\end{aligned} \tag{59}$$

Let us now consider the non-Gaussian covariance between pre- and post-reconstruction power spectra

$$\begin{aligned}C^{\rm T}_{gg**}(\boldsymbol{k}_1,\boldsymbol{k}_2) = \frac{1}{V^2}\sum_{i\neq j,k\neq l}&\langle\delta_{g,i}(\boldsymbol{k}_1)\delta_{g,j}\\ &(-\boldsymbol{k}_1)\delta_{*,k}(\boldsymbol{k}_2)\delta_{*,l}(-\boldsymbol{k}_2)\rangle_c.\end{aligned} \tag{60}$$

Since terms like

$$\sum_{i\neq j\neq l,i=k}\cdots = \sum_{i\neq j\neq l}\frac{1}{\bar{n}_g^2}n_{g,i}e^{-i\boldsymbol{k}_{12}\cdot\boldsymbol{x}_i}e^{-i\boldsymbol{k}_2\cdot\boldsymbol{s}_i}\delta_{g,j}(-\boldsymbol{k}_1)\delta_{*,l}(-\boldsymbol{k}_2), \tag{61}$$

cannot be expressed in terms of δ_g and δ_*, we instead expand the summation as follows (see Equations (17), (18) and (19) in Sugiyama et al. 2020)

$$\sum_{i\neq j,k\neq l} = \sum_{i,j,k,l} - \sum_{i=j,k,l} - \sum_{k=l,i,j} + \sum_{i=j,k=l}. \tag{62}$$

The first term is

$$\sum_{i,j,k,l}\cdots = \frac{1}{V}T^{\rm N}_{gg**}(\boldsymbol{k}_1,-\boldsymbol{k}_1,\boldsymbol{k}_2,-\boldsymbol{k}_2). \tag{63}$$

Using Equation (13) and

$$\delta_{*,i}(\boldsymbol{0}) \simeq \delta_{g,i}(\boldsymbol{0}) \qquad \delta_{*,i}(\boldsymbol{k}_1)\delta_{*,i}(\boldsymbol{k}_2) \simeq \frac{1}{\bar{n}_g}\delta_{*,i}(\boldsymbol{k}_{12}), \tag{64}$$

the second term expands as

$$\sum_{i=j,k,l}\cdots = \sum_{i\neq k\neq l} + \sum_{i=k,k\neq l} + \sum_{i=l,i\neq k} + \sum_{k=l,i\neq k} + \sum_{i=j=k} \tag{65}$$

$$= \frac{1}{V}\frac{1}{\bar{n}_g}\left\{B_{g**}(\boldsymbol{0},\boldsymbol{k}_2,-\boldsymbol{k}_2) + \frac{2}{\bar{n}_g}P_{**}(\boldsymbol{k}_2) + \frac{1}{\bar{n}_g}P_{g*}(\boldsymbol{0}) + \frac{1}{\bar{n}_g^2}\right\} \tag{66}$$

The third term expands as

$$\sum_{k=l,i,j}\cdots=\frac{1}{V}\frac{1}{\bar{n}_g}\Bigg\{B_{gg*}(\boldsymbol{k}_1,-\boldsymbol{k}_1,\boldsymbol{0})+\frac{2}{\bar{n}_g}P_{gg}(\boldsymbol{k}_2)+\frac{1}{\bar{n}_g}P_{g*}(\boldsymbol{0})+\frac{1}{\bar{n}_g^2}\Bigg\},\tag{67}$$

and the last term is given by

$$\sum_{i=j,k=l}\cdots=\frac{1}{V}\frac{1}{\bar{n}_g^2}\Bigg\{P_{g*}(\boldsymbol{0})+\frac{1}{\bar{n}_g}\Bigg\}.\tag{68}$$

Therefore, we obtain

$$\begin{aligned}C^{\rm T}_{gg**}(\boldsymbol{k}_1,\boldsymbol{k}_2)=&\frac{1}{V}T^{\rm N}_{gg**}(\boldsymbol{k}_1,-\boldsymbol{k}_1,\boldsymbol{k}_2,-\boldsymbol{k}_2)\\&-\frac{1}{V}\frac{1}{\bar{n}_g}\{B_{gg*}(\boldsymbol{k}_1,-\boldsymbol{k}_1,\boldsymbol{0})+B_{g**}(\boldsymbol{0},\boldsymbol{k}_2,-\boldsymbol{k}_2)\\&+\frac{2}{\bar{n}_g}P_{gg}(\boldsymbol{k}_1)+\frac{2}{\bar{n}_g}P_{**}(\boldsymbol{k}_2)+\frac{1}{\bar{n}_g}P_{g*}(\boldsymbol{0})+\frac{1}{\bar{n}_g^2}\Bigg\}.\end{aligned}\tag{69}$$

Using the fact that at the tree level

$$P_{gg}(\boldsymbol{k})=P_{**}(\boldsymbol{k})\qquad P_{g*}(\boldsymbol{0})=P_{gg}(\boldsymbol{0}),\tag{70}$$

and substituting Equations (45), (46) and (48) into the above formula, the final expression is written as

$$\begin{aligned}C^{\rm T}_{gg**}(\boldsymbol{k}_1,\boldsymbol{k}_2)=&\,C^{\rm T}_{gggg}(\boldsymbol{k}_1,\boldsymbol{k}_2)\\&+\frac{1}{V}\{[2R_2(-\boldsymbol{k}_1,\boldsymbol{k}_1-\boldsymbol{k}_2)P^{\rm N}_{gg}(\boldsymbol{k}_1)B^{\rm N}_{ggg}\\&\times(-\boldsymbol{k}_1,\boldsymbol{k}_2,\boldsymbol{k}_1-\boldsymbol{k}_2)+(\boldsymbol{k}_1\leftrightarrow-\boldsymbol{k}_1)]+(\boldsymbol{k}_2\leftrightarrow-\boldsymbol{k}_2)\}\\&+\frac{1}{V}\{4R_2(-\boldsymbol{k}_1,\boldsymbol{k}_1-\boldsymbol{k}_2)^2P^{\rm N}_{gg}(\boldsymbol{k}_1)^2P^{\rm N}_{gg}\\&\times(-\boldsymbol{k}_1+\boldsymbol{k}_2)+(\boldsymbol{k}_1\leftrightarrow-\boldsymbol{k}_1)\}\\&+\frac{1}{V}\{6R_3(-\boldsymbol{k}_1,\boldsymbol{k}_1,-\boldsymbol{k}_2)P^{\rm N}_{gg}(\boldsymbol{k}_1)^2P^{\rm N}_{gg}(\boldsymbol{k}_2)+(\boldsymbol{k}_2\leftrightarrow-\boldsymbol{k}_2)\}\\&+\frac{1}{V}\{2R_2(-\boldsymbol{k}_2,\boldsymbol{0})P^{\rm N}_{gg}(\boldsymbol{k}_2)B^{\rm N}_{ggg}(\boldsymbol{k}_1,-\boldsymbol{k}_1,\boldsymbol{0})+(\boldsymbol{k}_2\leftrightarrow-\boldsymbol{k}_2)\}\\&-\frac{1}{V}\frac{2}{\bar{n}_g}\{R_2(\boldsymbol{0},\boldsymbol{k}_2)P_{gg}(\boldsymbol{0})P^{\rm N}_{gg}(\boldsymbol{k}_2)+R_2(\boldsymbol{0},\boldsymbol{k}_2)P^{\rm N}_{gg}(\boldsymbol{0})P_{gg}(\boldsymbol{k}_2)\}.\end{aligned}\tag{71}$$

The last two lines vanish in the case when there are no modes larger than the periodic simulation box we are considering.

2.7. Numerical Implementation

In previous sections, we derived the covariance matrix of power spectrum estimators for a single mode. In the analysis, we will use the binned power spectrum projected in the Legendre basis, i.e., the power spectrum multipoles, namely,

$$\widehat{P}_\ell(k)=(2\ell+1)\sum_{\bar{\boldsymbol{k}}}\widehat{P}(\boldsymbol{k})\mathcal{L}_\ell(\hat{\boldsymbol{k}}\cdot\hat{\boldsymbol{\eta}}),\tag{72}$$

where $\boldsymbol{k}$ takes discrete values with the unit of fundamental frequency $k_f=2\pi/L$, and $\mathcal{L}_\ell$ is the ℓ-th order Legendre polynomial. Symbol $\sum_{\bar{\boldsymbol{k}}}$ represents the average of $\boldsymbol{k}$-modes inside a spherical shell with the wavenumber $|\boldsymbol{k}|$ satisfying $|\boldsymbol{k}|\in[k-\Delta k/2,\,k+\Delta k/2)$ and Δk the width of k-bins. This definition can be expressed in terms of a top-hat function Ξ_k

$$\begin{aligned}\sum_{\bar{\boldsymbol{k}}}&\equiv\sum_{\boldsymbol{k}'}\Xi_k(\boldsymbol{k}')\\\Xi_k(\boldsymbol{k}')&\equiv\begin{cases}\dfrac{1}{N_k} & \text{if } |\boldsymbol{k}'|\in[k-\Delta k/2,\,k+\Delta k/2)\\0 & \text{otherwise}\end{cases},\end{aligned}\tag{73}$$

with N_k the number of modes inside the spherical shell $N_k\simeq V_k/k_f^3$. Ξ_k is an even function and has the following properties

$$\sum_{\bar{\boldsymbol{k}}_2}g(\boldsymbol{k}_1,\boldsymbol{k}_2)\delta^K_{\boldsymbol{k}_{12}}=g(\boldsymbol{k}_1,-\boldsymbol{k}_1)\Xi_{k_2}(\boldsymbol{k}_1),\tag{74}$$

$$\sum_{\bar{\boldsymbol{k}}_1,\bar{\boldsymbol{k}}_2}g(\boldsymbol{k}_1,\boldsymbol{k}_2)\delta^K_{\boldsymbol{k}_{12}}=\frac{\delta^K_{k_1,k_2}}{N_{k_1}}\sum_{\bar{\boldsymbol{k}}_1}g(\boldsymbol{k}_1,-\boldsymbol{k}_1),\tag{75}$$

where g is an arbitrary function, and the 2nd equality assumes non-overlapping bins for k_1 and k_2. The two-argument Kronecker symbol $\delta^K_{k_1,k_2}$ is equal to 1 when $k_1=k_2$ and vanishes otherwise.

The Gaussian covariance matrix of power spectrum multipoles becomes

$$\begin{aligned}C^{\rm G}_{\ell_1\ell_2}(k_1,k_2)=&\,\delta^K_{k_1,k_2}\frac{2}{N_{k_1}}(2\ell_1+1)(2\ell_2+1)\\&\times\sum_{\bar{\boldsymbol{k}}_1}P^2(\boldsymbol{k}_1)\mathcal{L}_{\ell_1}(\hat{\boldsymbol{k}}_1\cdot\hat{\boldsymbol{\eta}})\mathcal{L}_{\ell_2}(\hat{\boldsymbol{k}}_1\cdot\hat{\boldsymbol{\eta}}),\end{aligned}\tag{76}$$

where P takes $P^{\rm N}_{gg}$, $P^{\rm N}_{**}$ and $P^{\rm N}_{g*}$ for the pre-, post- and cross-correlation covariance matrix, respectively. The non-Gaussian part is given by

$$\begin{aligned}C^{\rm T}_{\ell_1\ell_2}(k_1,k_2)=&\,(2\ell_1+1)(2\ell_2+1)\\&\times\sum_{\bar{\boldsymbol{k}}_1,\bar{\boldsymbol{k}}_2}C^{\rm T}(\boldsymbol{k}_1,\boldsymbol{k}_2)\mathcal{L}_{\ell_1}(\hat{\boldsymbol{k}}_1\cdot\hat{\boldsymbol{\eta}})\mathcal{L}_{\ell_2}(\hat{\boldsymbol{k}}_2\cdot\hat{\boldsymbol{\eta}}).\end{aligned}\tag{77}$$

Although the above two equations accurately capture the binning effect in the power spectrum measurement, we will adopt the continuous limit and the thin shell approximation to reduce the computational cost, i.e.,

$$\sum_{\bar{\boldsymbol{k}}}\to\int_{\bar{\boldsymbol{k}}}\to\int_{\hat{\boldsymbol{k}}}\equiv\int\frac{{\rm d}^2\hat{\boldsymbol{k}}}{4\pi}.\tag{78}$$

Therefore the Gaussian covariance matrix is given by

$$\begin{aligned}C^{\rm G}_{\ell_1\ell_2}(k_1,k_2)=&\,\delta^K_{k_1,k_2}\frac{2}{N_{k_1}}(2\ell_1+1)(2\ell_2+1)\\&\times\int_{\hat{\boldsymbol{k}}_1}P^2(\boldsymbol{k}_1)\mathcal{L}_{\ell_1}(\hat{\boldsymbol{k}}_1\cdot\hat{\boldsymbol{\eta}})\mathcal{L}_{\ell_2}(\hat{\boldsymbol{k}}_1\cdot\hat{\boldsymbol{\eta}}).\end{aligned}\tag{79}$$

In the calculation, we use the non-perturbative $P(\boldsymbol{k}_1)$ constructed by averaging over $\widehat{P}_0$, $\widehat{P}_2$ and $\widehat{P}_4$ measured from simulations. We note that we do not remove the binning effect for simplicity.

According to the rotational symmetry, the non-Gaussian part reduces to a 3D integration

$$C^{\rm T}_{\ell_1\ell_2}(k_1, k_2) = \frac{(2\ell_1+1)(2\ell_2+1)}{8\pi}\int_{-1}^{1} {\rm d}\mu_1 \int_{-1}^{1} {\rm d}\mu_2 \times \int_0^{2\pi} {\rm d}\phi\; C^{\rm T}(k_1, k_2, \mu_1, \mu_2, \phi)\mathcal{L}_{\ell_1}(\mu_1)\mathcal{L}_{\ell_2}(\mu_2). \tag{80}$$

3. Comparison with Simulations

To test the analytic covariance derived in the last section, we measure the numerical covariance matrix of power spectra multipoles from 15,000 Quijote halo catalogs[8] at redshift $z = 0.5$. Each simulation evolves 512^3 particles inside a periodic box of $1\,h^{-1}$ Gpc length with the initial condition set by 2LPT at $z = 127$ and the fiducial cosmology $\{\Omega_m, \Omega_b, h, n_s, \sigma_8, M_\nu\} = \{0.3175, 0.049, 0.6711, 0.9624, 0.834, 0\}$. Dark matter halos are identified using the FoF algorithm (Davis et al. 1985). In this work, we only consider halos with a mass range of $10^{13.1\text{–}14.0}\,h^{-1}M_\odot$, leading to the mean halo number density of $\bar{n}_h \simeq 2.918 \times 10^{-4}\,[h^{-1}\,{\rm Mpc}]^{-3}$. The linear bias is found to be $b_1 \simeq 1.85$, obtained by running fits to the power spectrum multipoles with the `Velocileptors` EPT code (Chen et al. 2021; Maus et al. 2024b).

We use the public code `pyrecon`[9] and `pypower`[10] to perform the density field reconstruction and power spectrum measurement (Hand et al. 2017), respectively. The reconstruction algorithm is summarized as the following steps

1. Interpolate halo particles on a 1000^3 mesh with a box size of $1000\,h^{-1}$ Mpc using the Cloud-In-Cell (CIC) scheme, then compute the overdensity and transform to Fourier space.
2. Smooth the overdensity field using the kernel defined in Equation (21) with $\Sigma_s = 10$, 15 and $20\,h^{-1}$ Mpc.
3. Assuming a fiducial value for the linear bias $b_{\rm fid} = b_1$ and the growth rate $f_{\rm fid} = f_{\rm true} = 0.7628$ or[11] $f_{\rm fid} = 0$, estimate the shift field on the grid by solving Equation (19).
4. Displace halo particles with the estimated shift field interpolated at the particle position with the CIC scheme to obtain the displaced data catalog.

[8] https://quijote-simulations.readthedocs.io/en/latest/halos.html
[9] https://github.com/cosmodesi/pyrecon
[10] https://github.com/cosmodesi/pypower
[11] The choice of $f_{\rm fid} = 0$ is usually adopted in perturbation theory calculations (e.g., Hikage et al. 2020a; Sugiyama 2024a) as it is not straightforward to obtain the analytic expression of the full 3D power spectrum expanded in Legendre polynomials when $\hat{\boldsymbol{k}}\cdot\hat{\boldsymbol{\eta}}$ appears in the denominator.

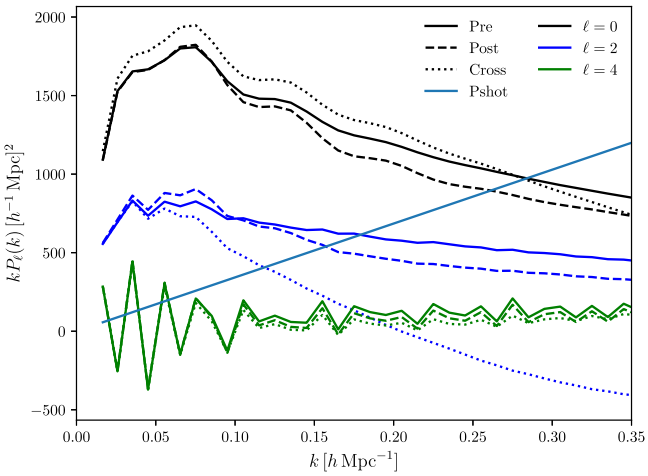

Figure 2. Solid lines, dashed lines and dotted lines show the measured pre- and post-recon power spectrum, and the cross power spectrum of our baseline, respectively. In this plot, the shot noise is removed from both the pre- and post-reconstruction power spectra, but is retained in the cross power spectrum.

5. Generate a random catalog with the number of randoms 50 times the number of halos. Random particles are then displaced in the same manner as halos to obtain the displaced random catalog.

The baseline reconstruction setting we use is $b_{\rm fid} = b_1$, $\Sigma_s = 15\,h^{-1}$ Mpc and $f_{\rm fid} = 0.7628$. The density field is then obtained by assigning particles on a 1000^3 mesh using the Triangular Shaped Cloud (TSC) scheme with the window function correction applied (Jing 2005). When painting particles on the mesh, we additionally use two interlaced grids (Sefusatti et al. 2016) shifted by 1/3 and 2/3 mesh cell size, respectively, to reduce the aliasing effect. Then, the pre-, post- and cross-power spectrum multipoles are estimated following Equations (49), (50), (52) and (72). In our analysis, we consider power spectrum measured between $k_{\rm min} = 0.01\,h\,{\rm Mpc}^{-1}$ and $k_{\rm max} = 0.35\,h\,{\rm Mpc}^{-1}$, with the k-bin size set by $\Delta k = 0.01\,h\,{\rm Mpc}^{-1}$. The measurements are shown in Figure 2.

The derivations presented in the last section have assumed $\bar{n}_g$ is a fixed number in the denominator. This is, however, not true because the number of halos varies between different realizations. So, we have two choices in the power spectrum estimation. One choice is to normalize the estimator using the number density measured in each realization, or the "local number density." Another choice is to use the ensemble averaged number density, or the "global number density." We found these two choices lead to almost the same mean power spectra but different numerical covariances especially at the small scale, with the "local number density" case showing smaller correlations in both the diagonal elements and the non-diagonal parts. This effect is very similar to the local average effect as pointed out by de Putter et al. (2012), but their

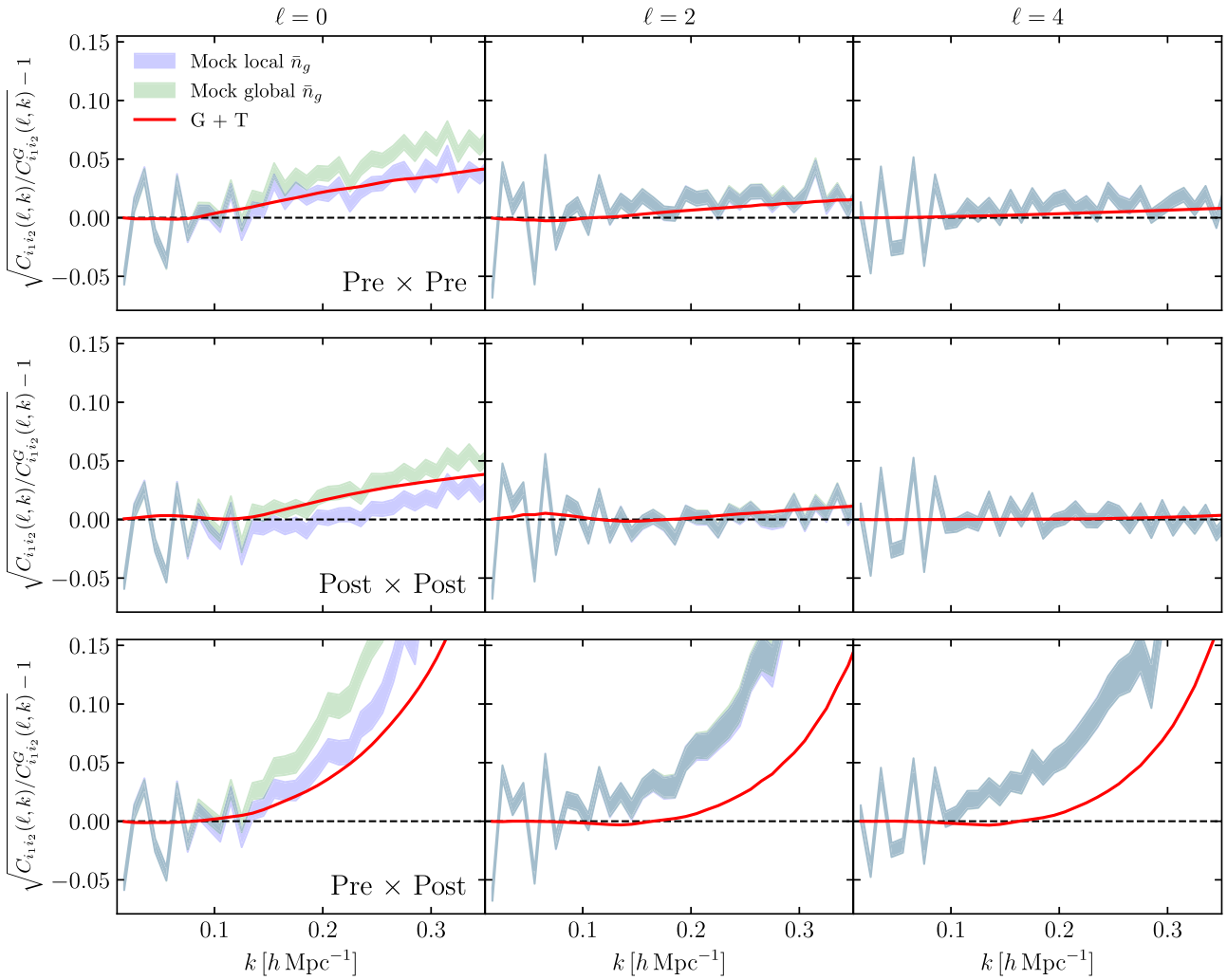

Figure 3. The relative difference in the square root of diagonal covariance elements compared with the Gaussian prediction. Red lines signify the result predicted by the analytic covariance matrix with the non-Gaussian contribution. Shaded bands show the numerical covariance matrix computed from 15,000 simulations.

physical origins are different. The latter is caused by the matter fluctuations at the survey scale, while in our case, the difference in the halo number density is caused by different initial conditions. On the other hand, comparing the analytic covariance with the "global number density" case is also not very consistent on the theory side, because it means the overdensity we defined can have fluctuations at the box scale. In any case, we will present both the "local number density" and the "global number density" measurements when comparing the theory prediction to simulations. The variation of number densities additionally leads to the variation of shot noise, but this effect has already been included in the derivation (see discussions in Smith 2009; Chan & Blot 2017; Wadekar & Scoccimarro 2020; Sugiyama et al. 2020).

The full covariance is represented by $C_{i_1i_2\ell_1\ell_2}(k_1, k_2)$, where i_1 and i_2 label either the pre- or post-reconstruction power spectrum. We will use symbol $C_{i_1i_2}(\ell, k)$ to denote the diagonal part, i.e., $\ell_1 = \ell_2 = \ell$ and $k_1 = k_2 = k$

$$C_{i_1i_2}(\ell, k) \equiv C_{i_1i_2\ell\ell}(k, k). \tag{81}$$

Figure 3 compares the diagonal part of covariance matrices between numerical covariances and analytic covariances using the baseline reconstruction setting. The 1σ error band is estimated by bootstrapping. As shown in the plot, the departure from the Gaussian prediction is around 5%[12] up to $k = 0.35\,h\,\mathrm{Mpc}^{-1}$ for the auto-correlation covariance. The post-reconstruction covariance agrees with the Gaussian prediction better compared to the pre-reconstruction.[13] This is expected, because reconstruction undoes the nonlinear

[12] This argument depends on the size of k-bins Δk.
[13] We remind the readers the Gaussian contribution is computed in the non-perturbative way, so any deviations show the pure trispectrum effect.

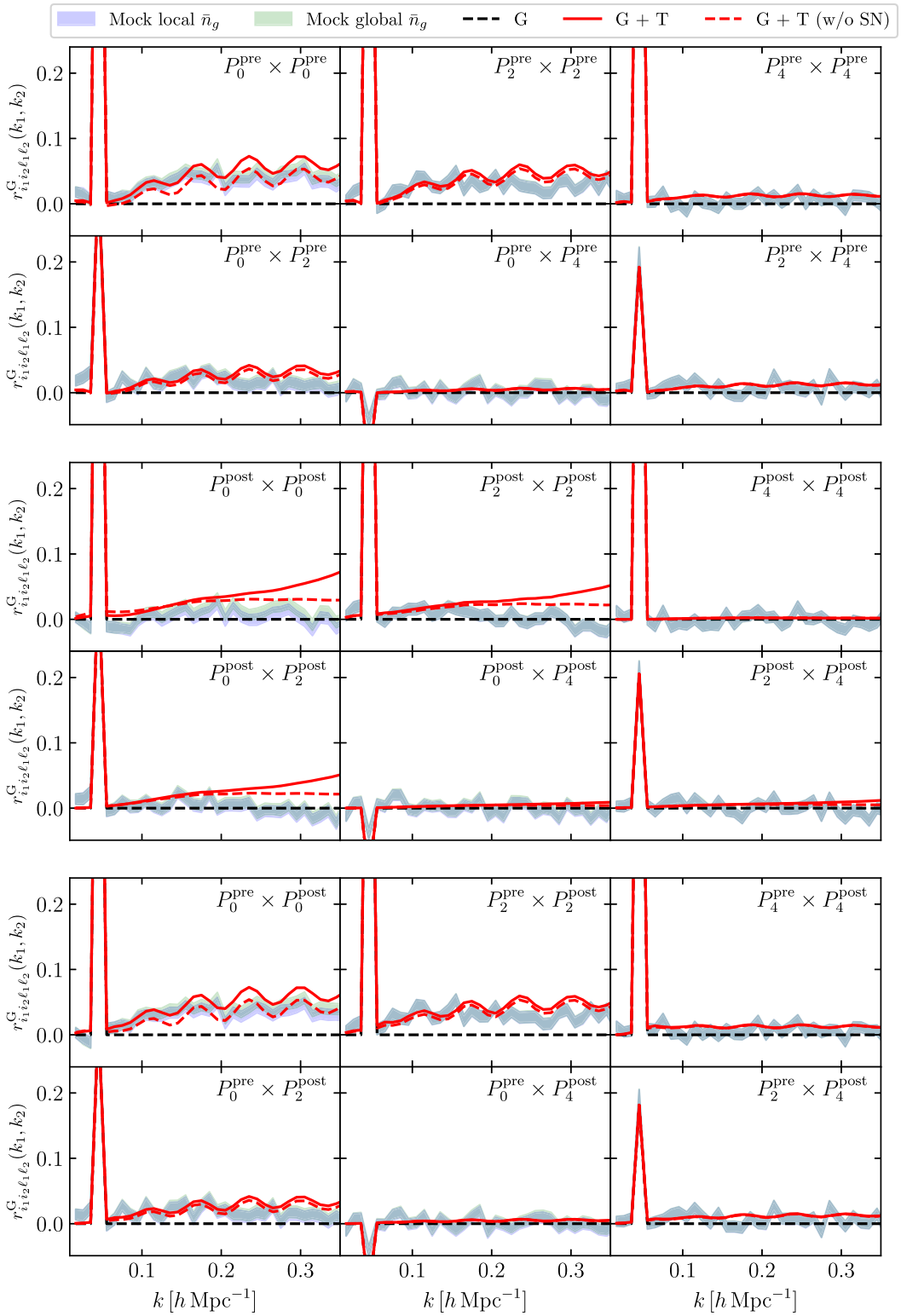

Figure 4. Covariance matrix normalized by the diagonal part of the Gaussian covariance with $k_2 = 0.045\,h\,{\rm Mpc}^{-1}$. Black dashed lines show the Gaussian analytic covariance. Red solid lines signify the non-Gaussian analytic covariance. Red dashed lines correspond to the non-Gaussian analytic covariance but excluding the shot noise contribution when calculating the $C^{\rm T}$ term. Blue and green bands are numerical covariance matrices estimated from 15,000 realizations.

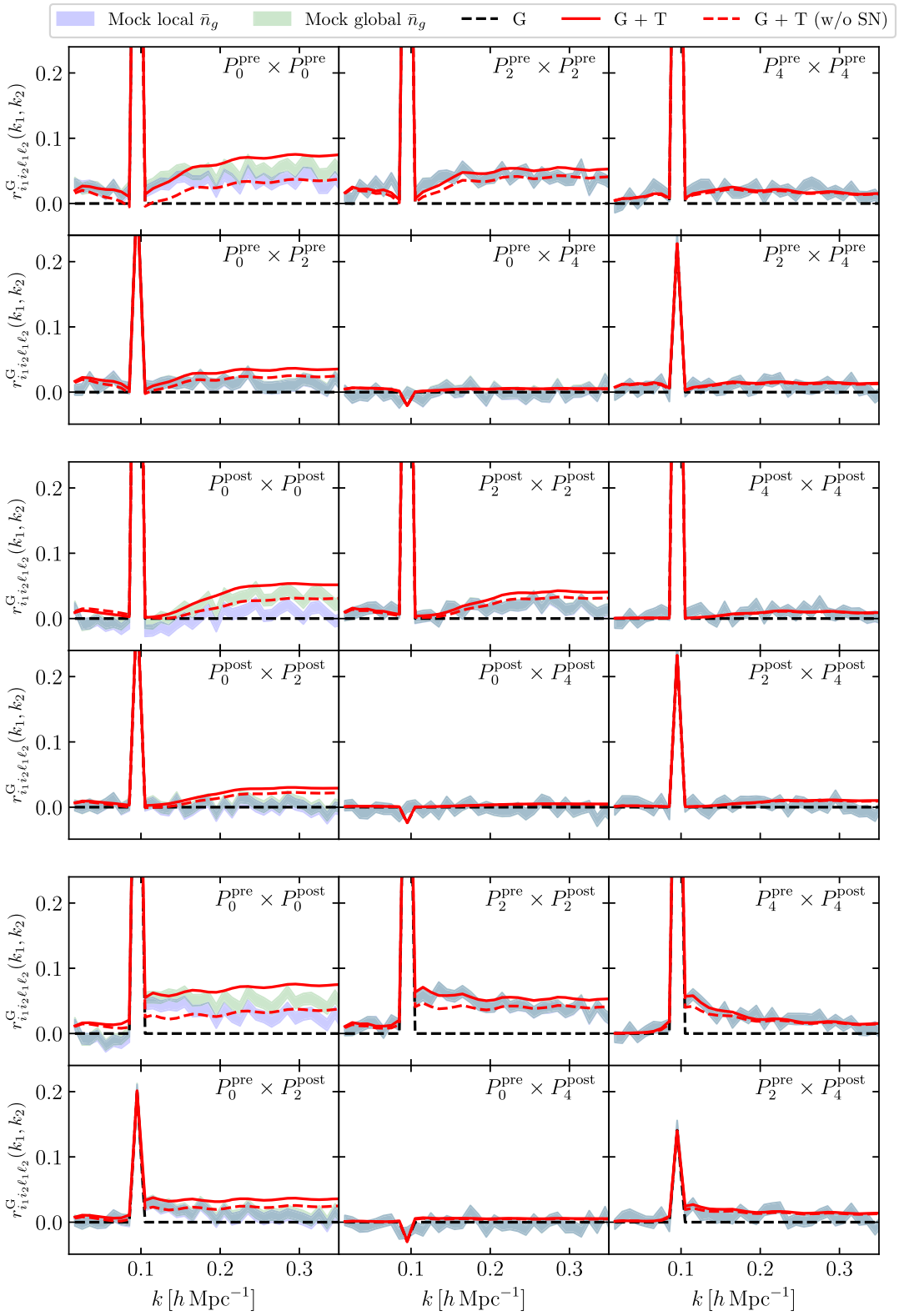

Figure 5. Similar to Figure 4, but with $k_2 = 0.095\,h\,{\rm Mpc}^{-1}$.

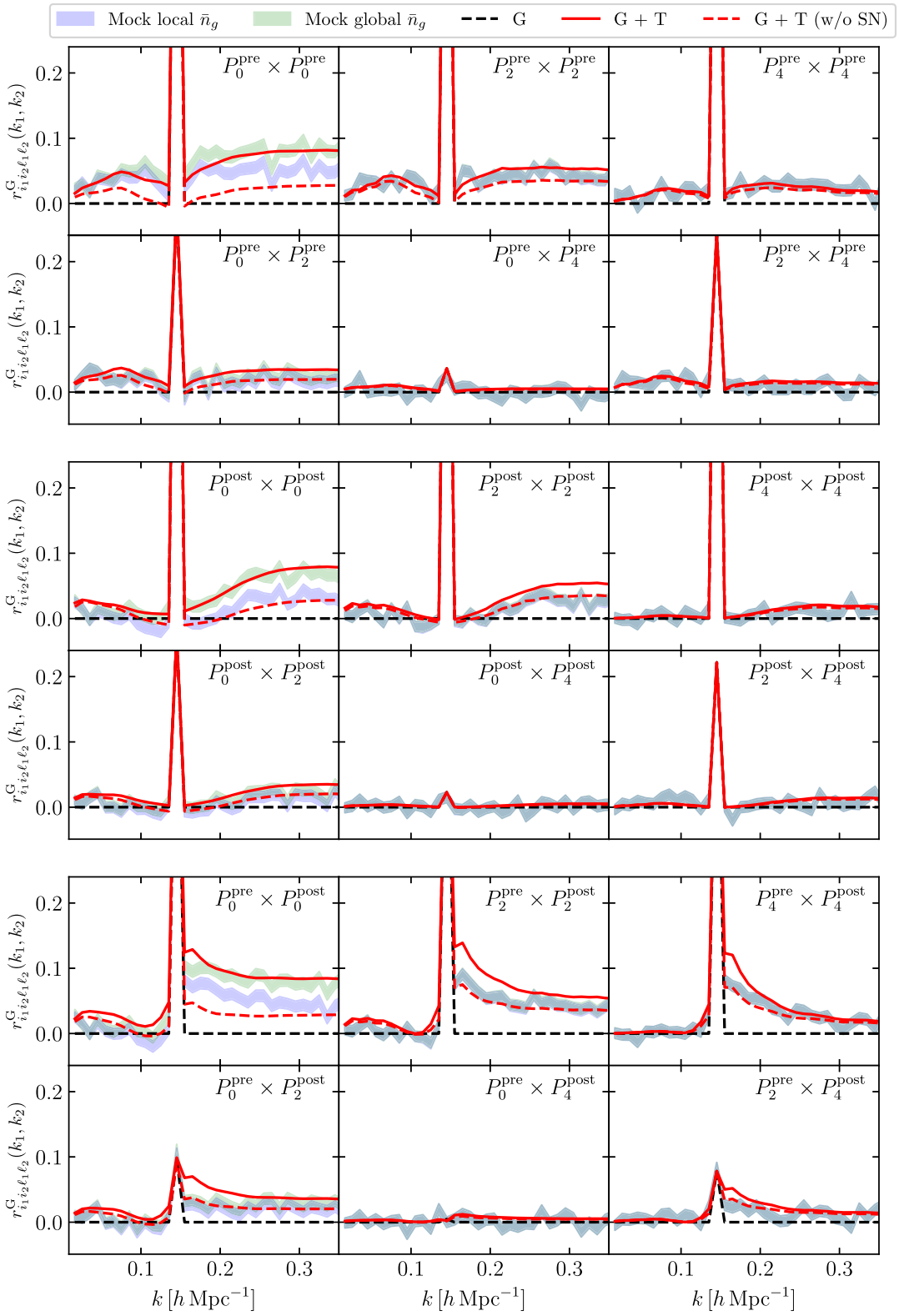

Figure 6. Similar to Figure 4, but with $k_2 = 0.145\,h\,{\rm Mpc}^{-1}$.

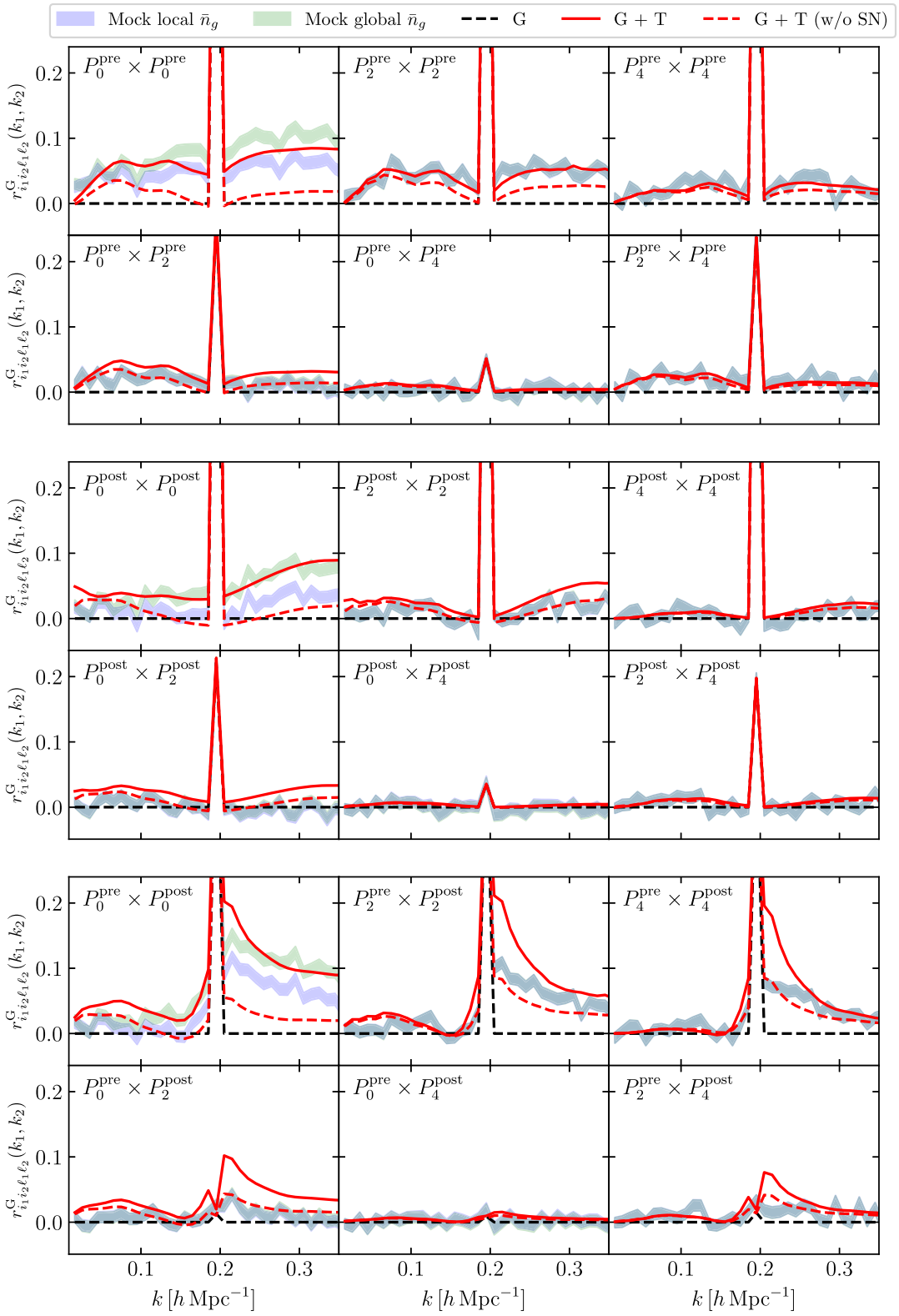

Figure 7. Similar to Figure 4, but with $k_2 = 0.195\,h\,{\rm Mpc}^{-1}$.

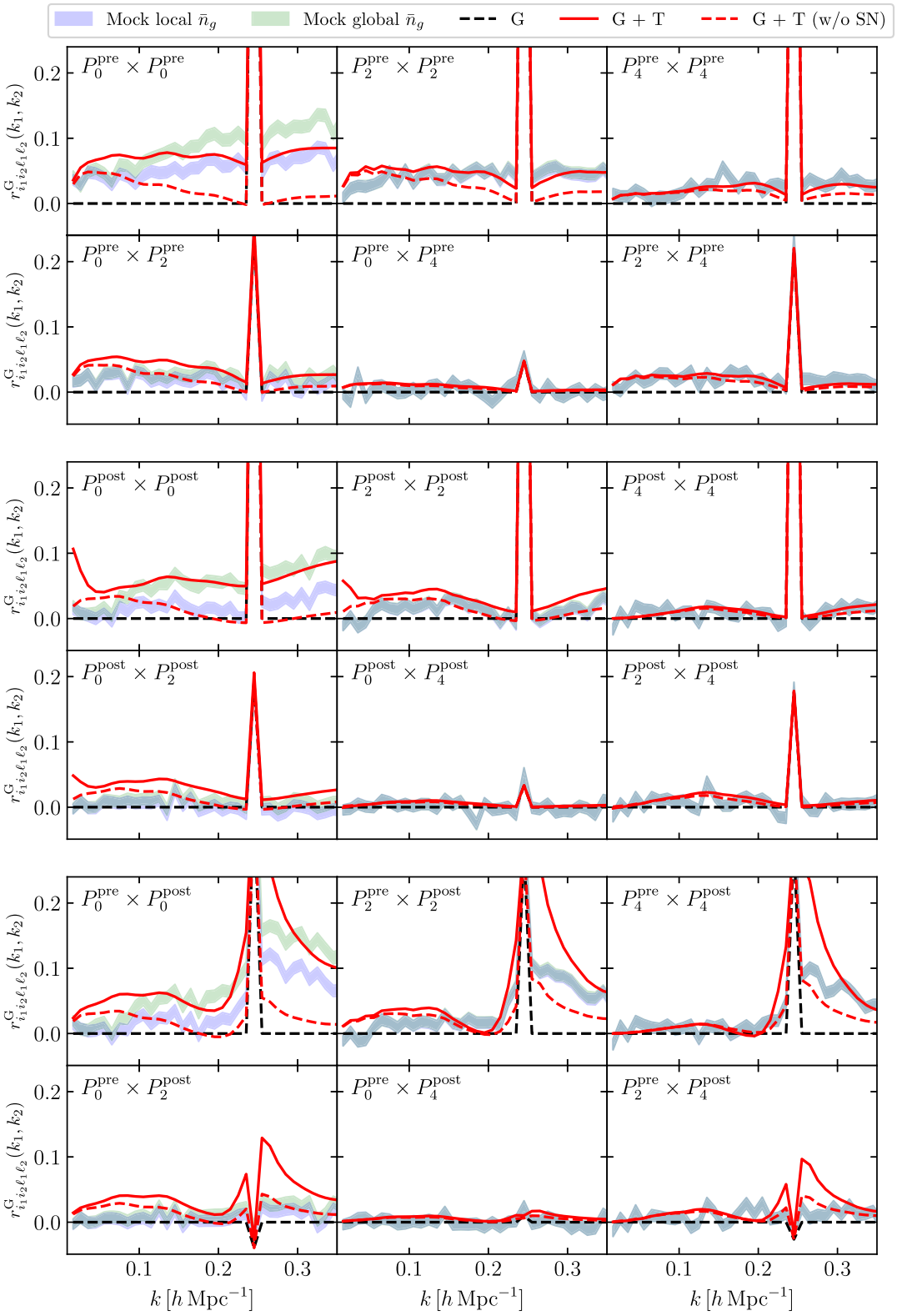

Figure 8. Similar to Figure 4, but with $k_2 = 0.245\,h\,{\rm Mpc}^{-1}$.

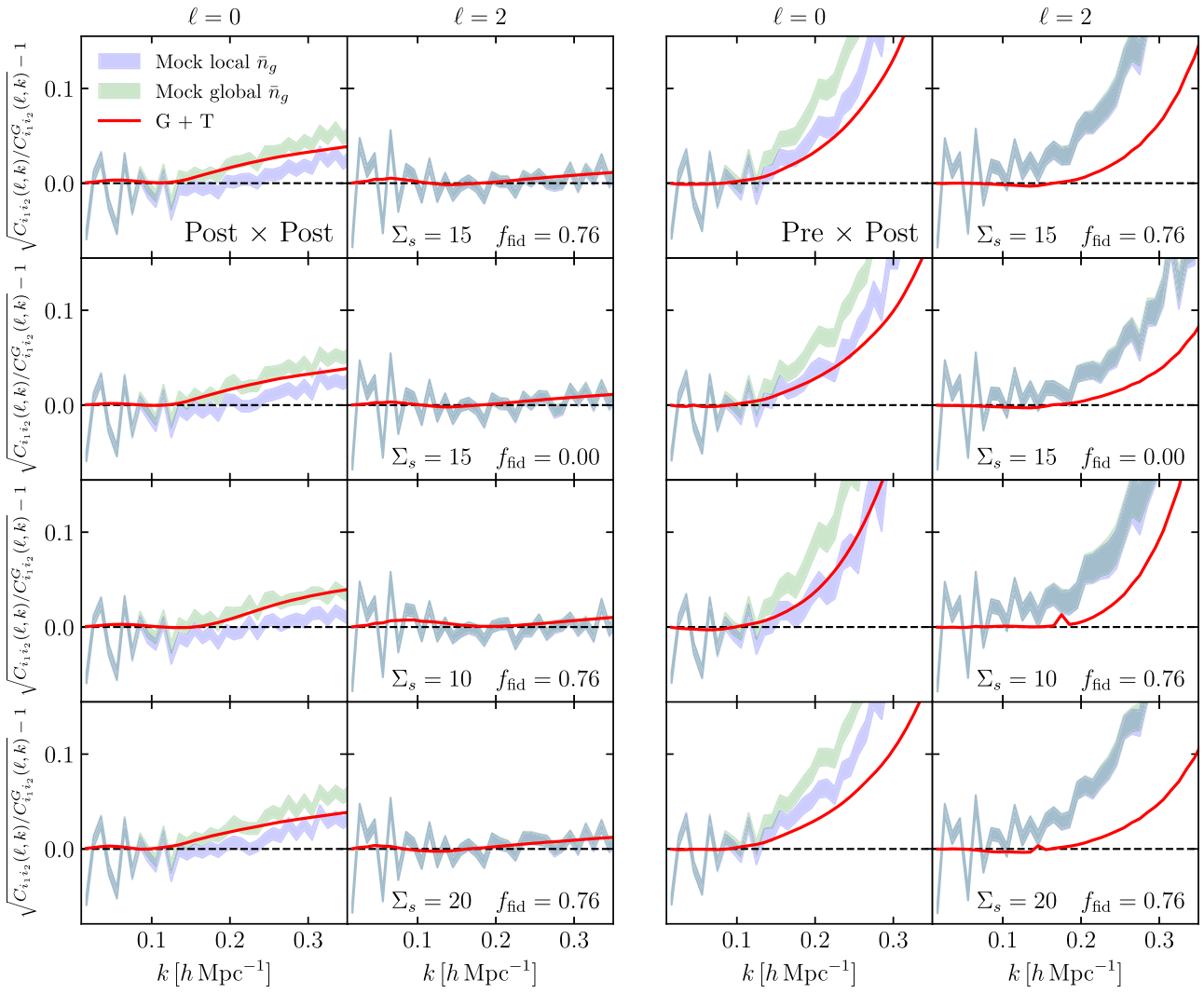

Figure 9. Similar to Figure 3, but comparing different reconstruction settings.

gravitational evolution, so that the induced correlations between measured power spectra are suppressed (Hikage et al. 2020b). However, the cross-correlation between pre- and post-reconstruction power spectra is much stronger compared to the Gaussian prediction, and the deviation exceeds 15% when k goes beyond $0.25\,h\,{\rm Mpc}^{-1}$. Adding the non-Gaussian contribution to the analytic covariance improves the agreement between the theoretical prediction and the numerical covariance especially in the auto-correlation covariance, while the theory still under-predicts the cross-correlation covariance.

To compare non-diagonal elements, we use symbol $r^{\rm G}_{i_1 i_2 \ell_1 \ell_2}(k_1, k_2)$ to represent the covariance matrix normalized by the Gaussian prediction

$$r^{\rm G}_{i_1 i_2 \ell_1 \ell_2}(k_1, k_2) \equiv \frac{C_{i_1 i_2 \ell_1 \ell_2}(k_1, k_2)}{\sqrt{C^{\rm G}_{i_1 i_1 \ell_1 \ell_1}(k_1, k_1) C^{\rm G}_{i_2 i_2 \ell_2 \ell_2}(k_2, k_2)}}. \quad (82)$$

Figures 4, 5, 6, 7 and 8 show $r^{\rm G}_{i_1 i_2 \ell_1 \ell_2}(k_1, k_2)$ at $k_2 = 0.045$, 0.095, 0.145, 0.195, $0.245\,h\,{\rm Mpc}^{-1}$, respectively. In each plot, we also display the non-Gaussian analytic covariance with the shot noise contribution set to zero. Overall, the agreement between the theory prediction and the numerical covariance is reasonably good. Even when $k > 0.15\,h\,{\rm Mpc}^{-1}$, the theory prediction still captures the shape of correlations between different k-bins. The non-Gaussian effect in the cross covariance is comparable to, or even stronger than, the pre-reconstruction covariance. According to the theoretical calculation, we conclude that this enhancement is due to the shot noise effect.

We also notice there are a few features appearing in the analytic covariance but not present in the numerical covariance. For example, the $P_0^{\rm post} \times P_0^{\rm post}$ block in Figure 8 shows peculiar enhancements in small k. It is likely caused by the second line in Equation (44), which diverges in the

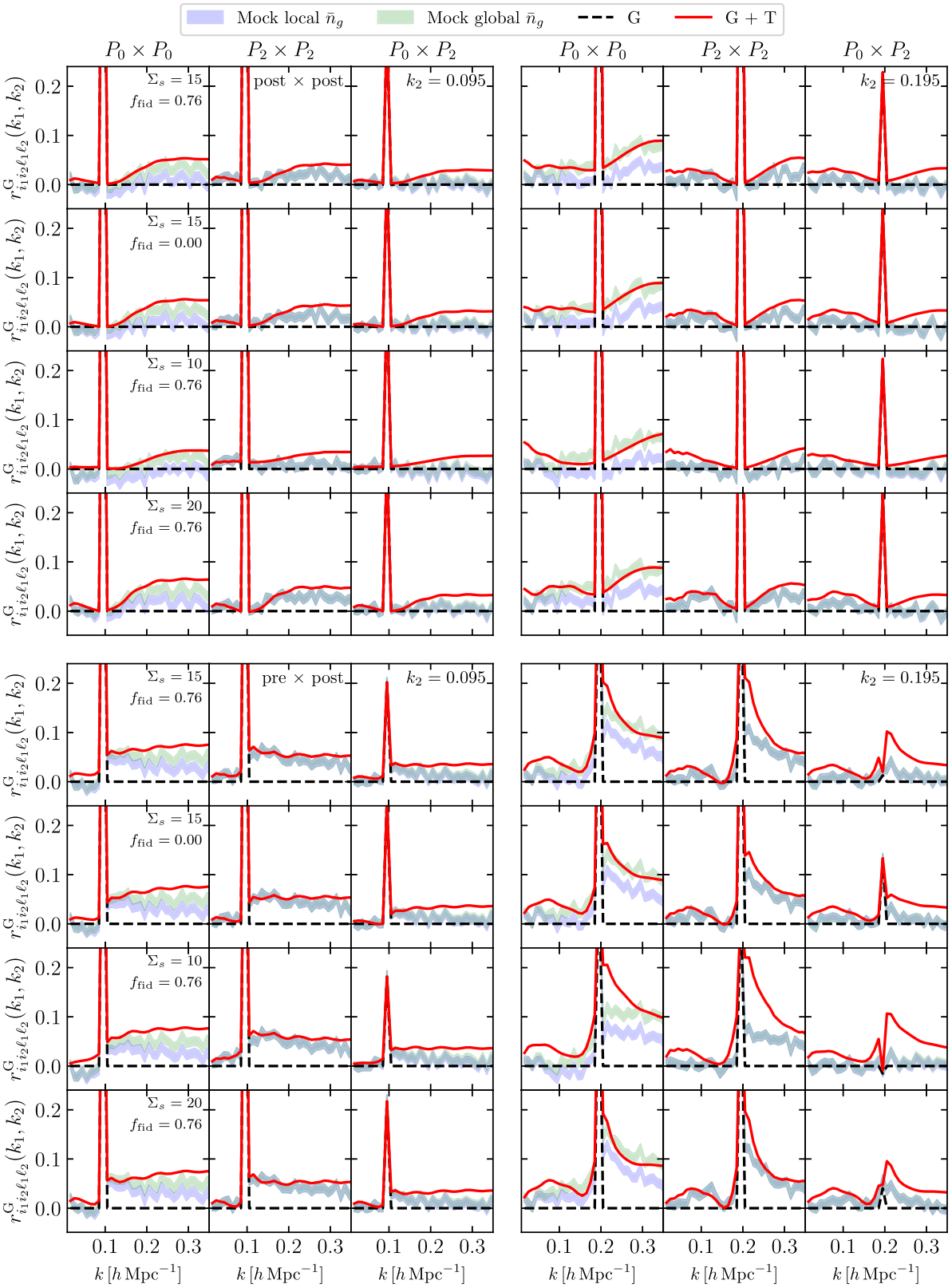

Figure 10. Similar to Figure 4, but comparing different reconstruction settings.

squeezed limit when $\boldsymbol{k}_3$ goes to $\mathbf{0}$ because $P_{gg}^{\rm N}(\boldsymbol{k}_3) \to$ const while $R_2(\boldsymbol{k}_2, \boldsymbol{k}_3) \to \infty$. In addition, at small scales, the theory strongly over-predicts the correlation when k_1 approaches k_2 in the cross-correlation covariance. This may be attributed to the IR-effect as pointed by Sugiyama (2024a), i.e., the cross-power spectra and its shot noise should damp exponentially due to the lack of IR-cancellation. However, deriving the full IR-resummation equation for the cross-correlation trispectrum is beyond the scope of this paper, and we leave it to future work.

We then study the change of numeric and analytic covariances by varying the smoothing scale and the fiducial growth rate. Results are shown in Figures 9 and 10. Changing $f_{\rm fid}$ mainly changes the quadruple contribution, and increasing the smoothing scale increases the correlations in the post-reconstruction power spectra while decreasing the correlations in the pre- and post-reconstruction cross covariance. This is because the post-reconstruction power spectrum recovers the pre-reconstruction power spectrum when $\Sigma_s \to \infty$, so that C_{gg**} reduces to C_{gggg}. The theory prediction is still in good agreement with the numeric covariance, and the theory matches the numerical covariance better when using a larger smoothing scale or a zero $f_{\rm fid}$.

4. Conclusion and Discussions

The reconstruction technique provides a useful tool to improve the measurement of the BAO signal and makes the standard ruler more robust by undoing the nonlinear gravitational evolution. This field level operation brings back information beyond the 2-point statistics but also complicates the analysis especially when combining with the pre-reconstruction statistics. This is because both the signal and the covariance are affected by higher-order statistics.

In this work, we build a theory model of the covariance matrix for the power spectra before and after the BAO reconstruction based on the recent theoretical progress in the reconstruction modeling (Sugiyama 2024a, 2024b, 2024c). We check the accuracy of our model against 15,000 halo mocks at redshift $z = 0.5$. We show that the diagonal part of the covariance matrix is well described by the Gaussian prediction, with the maximum deviation of 5% for the pre- and post-reconstruction auto covariance. However, the cross covariance between pre- and post-reconstruction power spectra deviates from the Gaussian prediction quickly when $k > 0.1\,h\,{\rm Mpc}^{-1}$ and achieves 15% at $k = 0.25\,h\,{\rm Mpc}^{-1}$. In addition, the non-Gaussian effect in the cross covariance is comparable to, or even stronger than, the pre-reconstruction covariance. We find that adding the non-Gaussian covariance predicted by the perturbation theory leads to a better agreement with the numeric covariance up to $k \simeq 0.15\,h\,{\rm Mpc}^{-1}$, and the shot noise effect has a very large contribution at small scales. When $k > 0.15\,h\,{\rm Mpc}^{-1}$, the theory prediction still captures the shape of correlations between different k-bins, but over-predicts the correlation near the diagonal elements in the cross covariance. We also test the model with different smoothing scales and different fiducial growth rates when doing the reconstruction, and we find similar agreements with the numeric covariance.

In future work, we plan to extend the model to account for the IR-resummation effect. It will also be interesting to extend the calculation to multiple galaxy populations (Ebina & White 2024b; Mergulhão et al. 2024; Zhao et al. 2024) and correlation functions (Philcox et al. 2020; Rashkovetskyi et al. 2023), and compare the covariance matrix performance at the parameter level (Alves et al. 2024; Forero-Sanchez et al. 2024; Rashkovetskyi et al. 2024). The impact of the survey window function (Wadekar & Scoccimarro 2020), the local average effect (de Putter et al. 2012), the super survey effect (Takada & Hu 2013) and the fiber collision affects (Pinon et al. 2024) on covariance matrices are also interesting topics. This work provides a useful reference for future extensions.

Acknowledgments

R.Z. thanks Nathan Findlay for the inspiration of using n_* to represent the post-reconstruction field. R.Z., Y.W. and G.B.Z. are supported by National Key R&D Program of China No. 2023YFA1607803, National Natural Science Foundation of China (NSFC, grant No. 11925303), and by the CAS Project for Young Scientists in Basic Research (No. YSBR-092). R.Z. is also supported by the Chinese Scholarship Council (CSC) and the University of Portsmouth. K.K. is supported by the STFC grant ST/W001225/1. Y.W. is also supported by National Natural Science Foundation of China (NSFC, grant Nos. 12273048 and 12422301), by National Key R&D Program of China No. 2022YFF0503404, by the Youth Innovation Promotion Association CAS, and by the Nebula Talents Program of NAOC. G.B.Z. is also supported by science research grants from the China Manned Space Project with No. CMS-CSST-2021-B01, and the New Cornerstone Science Foundation through the XPLORER prize. Numerical computations were done on the Sciama High Performance Compute (HPC) cluster which is supported by the ICG, SEPNet and the University of Portsmouth. For the purpose of open access, the authors have applied a Creative Commons Attribution (CC BY) licence to any Author Accepted Manuscript version arising.

Appendix
Perturbation Theory Before Reconstruction

The galaxy density field in redshift space can be expanded perturbatively

$$\delta_g^{(n)}(\boldsymbol{k}) = \int_{\boldsymbol{k}=\boldsymbol{p}_{1\cdots n}} Z_n(\boldsymbol{p}_1,\cdots,\boldsymbol{p}_n)\delta_L(\boldsymbol{p}_1)\cdots\delta_L(\boldsymbol{p}_n), \qquad \text{(A1)}$$

where we have adopted the EdS-approximation, with δ_L the linear matter density field evaluated at the observation redshift

and Z_n the n-th order perturbation kernel. In this work, we use the "descendants" bias basis defined in Perko et al. (2016) and assume $\tilde{c}_{\delta,1} = b_1$, $\tilde{c}_{\delta,2} = 1$, $\tilde{c}_{\delta,3} = 1$, with all other bias parameters set to 0. The tree-level bispectrum and trispectrum are given by Goroff et al. (1986)

$$B_{ggg}(\boldsymbol{k}_1, \boldsymbol{k}_2, \boldsymbol{k}_3) = 2Z_1(\boldsymbol{k}_1)Z_1(\boldsymbol{k}_2)Z_2(\boldsymbol{k}_1, \boldsymbol{k}_2)P_L(k_1)P_L(k_2) + (2\ \text{cyc.})\,, \tag{A2}$$

$$\begin{aligned} T_{gggg}(\boldsymbol{k}_1, \boldsymbol{k}_2, \boldsymbol{k}_3, \boldsymbol{k}_4) &= 4Z_1(\boldsymbol{k}_1)Z_1(\boldsymbol{k}_2)Z_2(-\boldsymbol{k}_1, \boldsymbol{k}_{14})Z_2 \\ &\times (-\boldsymbol{k}_2, \boldsymbol{k}_{23})P_L(k_1)P_L(k_2)P_L(k_{14}) + (11\ \text{perm.}) \\ &+ 6Z_1(\boldsymbol{k}_1)Z_1(\boldsymbol{k}_2)Z_1(\boldsymbol{k}_3)Z_3(\boldsymbol{k}_1, \boldsymbol{k}_2, \boldsymbol{k}_3)P_L \\ &\times (k_1)P_L(k_2)P_L(k_3) + (3\ \text{cyc.}). \end{aligned} \tag{A3}$$

The full power spectrum, bispectrum and trispectrum with the shot noise effect are given by Sugiyama et al. (2020) and Sugiyama (2024b). We copied these expressions in the following

$$P^{\mathrm{N}}_{gg}(\boldsymbol{k}) = P_{gg}(\boldsymbol{k}) + \frac{1}{\bar{n}_g}, \tag{A4}$$

$$B^{\mathrm{N}}_{ggg}(\boldsymbol{k}_1, \boldsymbol{k}_2, \boldsymbol{k}_3) = B_{ggg}(\boldsymbol{k}_1, \boldsymbol{k}_2, \boldsymbol{k}_3) + \frac{1}{\bar{n}_g}[P_{gg}(\boldsymbol{k}_1) + P_{gg}(\boldsymbol{k}_2) + P_{gg}(\boldsymbol{k}_3)] + \frac{1}{\bar{n}_g^2}, \tag{A5}$$

$$B^{\mathrm{N12}}_{ggg}(\boldsymbol{k}_1, \boldsymbol{k}_2, \boldsymbol{k}_3) = B_{ggg}(\boldsymbol{k}_1, \boldsymbol{k}_2, \boldsymbol{k}_3) + \frac{1}{\bar{n}_g}[P_{gg}(\boldsymbol{k}_1) + P_{gg}(\boldsymbol{k}_2)], \tag{A6}$$

$$\begin{aligned} T^{\mathrm{N}}_{gggg}(\boldsymbol{k}_1, \boldsymbol{k}_2, \boldsymbol{k}_3, \boldsymbol{k}_4) &= T_{gggg}(\boldsymbol{k}_1, \boldsymbol{k}_2, \boldsymbol{k}_3, \boldsymbol{k}_4) \\ &+ \frac{1}{\bar{n}_g}[B_{ggg}(-\boldsymbol{k}_{12}, \boldsymbol{k}_1, \boldsymbol{k}_2) \\ &+ B_{ggg}(-\boldsymbol{k}_{13}, \boldsymbol{k}_1, \boldsymbol{k}_3) + B_{ggg}(-\boldsymbol{k}_{14}, \boldsymbol{k}_1, \boldsymbol{k}_4) \\ &+ B_{ggg}(-\boldsymbol{k}_{23}, \boldsymbol{k}_2, \boldsymbol{k}_3) + B_{ggg}(-\boldsymbol{k}_{24}, \boldsymbol{k}_2, \boldsymbol{k}_4) \\ &+ B_{ggg}(-\boldsymbol{k}_{34}, \boldsymbol{k}_3, \boldsymbol{k}_4)] \\ &+ \frac{1}{\bar{n}_g^2}[P_{gg}(\boldsymbol{k}_1) + P_{gg}(\boldsymbol{k}_2) + P_{gg}(\boldsymbol{k}_3) + P_{gg}(\boldsymbol{k}_4) + P_{gg}(\boldsymbol{k}_{12}) \\ &+ P_{gg}(\boldsymbol{k}_{13}) + P_{gg}(\boldsymbol{k}_{14})] + \frac{1}{\bar{n}_g^3}. \end{aligned} \tag{A7}$$

ORCID iDs

Ruiyang Zhao https://orcid.org/0000-0002-7284-7265

References

Adame, A. G., Aguilar, J.DESI Collaboration, et al. 2024a, arXiv:2404.03000
Adame, A. G., DESI Collaboration, Aguilar, J., et al. 2024b, arXiv:2404.03002
Alam, S., Ata, M., Bailey, S., et al. 2017, MNRAS, 470, 2617
Alam, S., Aubert, M., Avila, S., et al. 2021, PhRvD, 103, 083533
Alves, O., et al. 2024, Analytical covariance matrices of DESI galaxy power spectra, in preparation
Baumann, D., Nicolis, A., Senatore, L., & Zaldarriaga, M. 2012, JCAP, 07, 051
Behera, J., Rezaie, M., Samushia, L., & Ereza, J. 2024, MNRAS, 531, 3326
Bertolini, D., Schutz, K., Solon, M. P., Walsh, J. R., & Zurek, K. M. 2016, PhRvD, 93, 123505
Beutler, F., Blake, C., Colless, M., et al. 2011, MNRAS, 416, 3017
Carrasco, J. J. M., Hertzberg, M. P., & Senatore, L. 2012, JHEP, 09, 082
Chan, K. C., & Blot, L. 2017, PhRvD, 96, 023528
Chen, S.-F., Vlah, Z., Castorina, E., & White, M. 2021, JCAP, 03, 100
Chen, S.-F., Vlah, Z., & White, M. 2019, JCAP, 09, 017
Chen, S.-F., Vlah, Z., & White, M. 2024a, arXiv:2406.00103
Chen, S.-F., Howlett, C., White, M., et al. 2024b, arXiv:2402.14070
Cole, S., Percival, W. J., Peacock, J. A., et al. 2005, MNRAS, 362, 505
Crocce, M., & Scoccimarro, R. 2006, PhRvD, 73, 063519
D'Amico, G., Donath, Y., Lewandowski, M., Senatore, L., & Zhang, P. 2024, JCAP, 05, 059
D'Amico, G., Gleyzes, J., Kokron, N., et al. 2020, JCAP, 05, 005
Davis, M., Efstathiou, G., Frenk, C. S., & White, S. D. M. 1985, ApJ, 292, 371
de Putter, R., Wagner, C., Mena, O., Verde, L., & Percival, W. 2012, JCAP, 04, 019
DESI Collaboration, Aghamousa, A., Aguilar, J., et al. 2016, arXiv:1611.00036
Desjacques, V., Jeong, D., & Schmidt, F. 2018, JCAP, 12, 035
Ebina, H., & White, M. 2024a, arXiv:2409.17133
Ebina, H., & White, M. 2024b, JCAP, 06, 052
Eggemeier, A., Scoccimarro, R., & Smith, R. E. 2019, PhRvD, 99, 123514
Eisenstein, D. J., Seo, H.-j., & White, M. J. 2007, ApJ, 664, 660
Eisenstein, D. J., Zehavi, I., Hogg, D. W., et al. 2005, ApJ, 633, 560
Feldman, H. A., Kaiser, N., & Peacock, J. A. 1994, ApJ, 426, 23
Feng, Y., Chu, M.-Y., Seljak, U., & McDonald, P. 2016, MNRAS, 463, 2273
Flöss, T., & Meerburg, P. D. 2024, JCAP, 02, 031
Forero-Sanchez, et al. 2024, Analytical and EZmock covariance validation for the DESI 2024 results, in preparation
Gil-Marín, H., Percival, W. J., Verde, L., et al. 2017, MNRAS, 465, 1757
Goroff, M. H., Grinstein, B., Rey, S. J., & Wise, M. B. 1986, ApJ, 311, 6
Gualdi, D., Gil-Marín, H. E., & Verde, L. 2021, JCAP, 07, 008
Hahn, C., Eickenberg, M., Ho, S., et al. 2024, PhRvD, 109, 083534
Hand, N., Li, Y., Slepian, Z., & Seljak, U. 2017, JCAP, 07, 002
Hartlap, J., Simon, P., & Schneider, P. 2007, A&A, 464, 399
Hikage, C., Koyama, K., & Heavens, A. 2017, PhRvD, 96, 043513
Hikage, C., Koyama, K., & Takahashi, R. 2020a, PhRvD, 101, 043510
Hikage, C., Takahashi, R., & Koyama, K. 2020b, PhRvD, 102, 083514
Ivanov, M. M., Simonović, M., & Zaldarriaga, M. 2020, JCAP, 05, 042
Jing, Y. P. 2005, ApJ, 620, 559
Kaiser, N. 1987, MNRAS, 227, 1
Kitaura, F.-S., Rodríguez-Torres, S., Chuang, C.-H., et al. 2016, MNRAS, 456, 4156
Laureijs, R., Amiaux, J., Arduini, S., et al. 2011, arXiv:1110.3193
Leonard, W. O., Slepian, Z., & Hou, J. 2024, arXiv:2402.15510
Maus, M., Chen, S., White, M., et al. 2024b, arXiv:2404.07312
Maus, M., Lai, Y., Noriega, H. E., et al. 2024a, arXiv:2404.07272
Meiksin, A., & White, M. J. 1999, MNRAS, 308, 1179
Mergulhão, T., Rubira, H., & Voivodic, R. 2024, JCAP, 01, 008
Mohammed, I., Seljak, U., & Vlah, Z. 2017, MNRAS, 466, 780
Novell-Masot, S., Gualdi, D., Gil-Marín, H., & Verde, L. 2023, JCAP, 11, 044
Ota, A., Seo, H.-J., Saito, S., & Beutler, F. 2021, PhRvD, 104, 123508
Peacock, J. A., Cole, S., Norberg, P., et al. 2001, Nature, 410, 169
Pearson, D. W., & Samushia, L. 2018, MNRAS, 478, 4500
Percival, W. J., Friedrich, O., Sellentin, E., & Heavens, A. 2022, MNRAS, 510, 3207
Percival, W. J., Ross, A. J., Sánchez, A. G., et al. 2014, MNRAS, 439, 2531
Perko, A., Senatore, L., Jennings, E., & Wechsler, R. H. 2016, arXiv:1610.09321
Philcox, O. H. E., Eisenstein, D. J., O'Connell, R., & Wiegand, A. 2020, MNRAS, 491, 3290
Philcox, O. H. E., & Ereza, J. 2024, arXiv:2401.09523
Philcox, O. H. E., Hou, J., & Slepian, Z. 2021, arXiv:2108.01670
Philcox, O. H. E., Ivanov, M. M., Cabass, G., et al. 2022, PhRvD, 106, 043530
Pinon, M., de Mattia, A., McDonald, P., et al. 2024, arXiv:2406.04804

Rashkovetskyi, M., Eisenstein, D. J., Aguilar, J. N., et al. 2023, MNRAS, 524, 3894
Rashkovetskyi, M., Forero-Sánchez, D., de Mattia, A., et al. 2024, arXiv:2404.03007
Schlegel, D. J., Kollmeier, J. A., Aldering, G., et al. 2022, arXiv:2209.04322
Schmittfull, M., Feng, Y., Beutler, F., Sherwin, B., & Chu, M. Y. 2015, PhRvD, 92, 123522
Scoccimarro, R., Zaldarriaga, M., & Hui, L. 1999, ApJ, 527, 1
Sefusatti, E., Crocce, M., Scoccimarro, R., & Couchman, H. 2016, MNRAS, 460, 3624
Seo, H.-J., Beutler, F., Ross, A. J., & Saito, S. 2016, MNRAS, 460, 2453
Shirasaki, M., Sugiyama, N. S., Takahashi, R., & Kitaura, F.-S. 2021, PhRvD, 103, 023506
Smith, R. E. 2009, MNRAS, 400, 851
Spaar, S., & Zhang, P. 2023, arXiv:2312.15164
Sugiyama, N. 2024a, PhRvD, 110, 063528
Sugiyama, N. 2024b, arXiv:2403.18262
Sugiyama, N. 2024c, arXiv:2406.01001
Sugiyama, N. S., Saito, S., Beutler, F., & Seo, H.-J. 2019, MNRAS, 484, 364
Sugiyama, N. S., Saito, S., Beutler, F., & Seo, H.-J. 2020, MNRAS, 497, 1684
Sugiyama, N. S., Yamauchi, D., Kobayashi, T., et al. 2023, MNRAS, 524, 1651
Takada, M., & Hu, W. 2013, PhRvD, 87, 123504
Takada, M., Ellis, R. S., Chiba, M., et al. 2014, PASJ, 66, R1
Taruya, A., Nishimichi, T., & Saito, S. 2010, PhRvD, 82, 063522
Villaescusa-Navarro, F., Hahn, C., Massara, E., et al. 2020, ApJS, 250, 2
Vlah, Z., White, M., & Aviles, A. 2015, JCAP, 09, 014
Wadekar, D., Ivanov, M. M., & Scoccimarro, R. 2020, PhRvD, 102, 123521
Wadekar, D., & Scoccimarro, R. 2020, PhRvD, 102, 123517
Wang, M. S., Beutler, F., & Sugiyama, N. S. 2023, JOSS, 8, 5571
Wang, Y., Zhai, Z., Alavi, A., et al. 2022, ApJ, 928, 1
Wang, Y., Zhao, R., Zhai, Z., et al. 2024a, ApJ, 966, 35
Wang, Y., Zhao, G., Koyama, K., et al. 2024b, CmPhy, 7, 130
White, M. 2015, MNRAS, 450, 3822
Zang, S.-H., & Zhu, H.-M. 2024, ApJ, 961, 160
Zhao, C., Chuang, C.-H., Bautista, J., et al. 2021, MNRAS, 503, 1149
Zhao, R., Mu, X., Gsponer, R., et al. 2024, MNRAS, 532, 783
Zhu, H.-M., Yu, Y., & Pen, U.-L. 2018, PhRvD, 97, 043502